Time-Resolved Operando Insights into the Tunable Selectivity of Cu-Zn Nanocubes during Pulsed CO_2 Electroreduction

Author list

Antonia Herzog[1,†], Martina Rüscher[1], Hyo Sang Jeon[1], Janis Timoshenko[1], Clara Rettenmaier[1], Uta Hejral[1], Earl M. Davis[1], F. T. Haase[1], David Kordus[1], Stefanie Kühl[1], Wiebke Frandsen[1], Arno Bergmann[1]*, Beatriz Roldan Cuenya[1]*

Affiliations

[1]Department of Interface Science, Fritz-Haber Institute of the Max-Planck Society, 14195 Berlin, Germany

[†]Present address: Massachusetts Institute of Technology, Research Laboratory of Electronics, 77 Massachusetts Ave, Cambridge, MA 02139, USA

Corresponding authors

*abergmann@fhi-berlin.mpg.de, roldan@fhi-berlin.mpg.de

Supplementary Notes

Supplementary Note 1. Calculation of the Faradaic efficiencies for gas and liquid products.

The Faradaic efficiencies (FEs) of the gas products were calculated as:

$$FE_x = \frac{\dot{V}\, C_x\, z_x\, F}{V_M\, j_{total}\, \dfrac{t_c}{t_c + t_a}} \cdot 100\%$$

and the FEs for liquid products was calculated as:

$$FE_x = \frac{V\, \Delta C_x\, z_x\, F}{\Delta Q} \cdot 100\%$$

FE_x: Faradaic efficiency of product x

$\dot{V}$: Flow rate of CO_2 / L s^{-1}

C_x: Volume-fraction of the product x detected by GC

z_x: Electrons transferred for reduction to product x

F: Faradaic constant / 96485 C mol^{-1}

V_M: Molar volume / 24.5 L mol^{-1}

j_{total}: Total current density during CO_2 electrolysis in the cathodic part / A cm^{-2}

t_c: Duration of the cathodic pulse / s

t_a: Duration of the anodic pulse / s

ΔC_x: Accumulated concentration of product x detected by HPLC or liquid GC / mol L^{-1}

ΔQ: Total charge transfer during the electrolysis at constant potential or current / C

V: Volume of the electrolyte / L.

For the gas products, $\dot{V}$ can be obtained by a universal flow meter (ADM 1000, Agilent Technologies) at the exit of the H-type cell, and C_x is given based on a previous calibration of the GC. A equals 2 cm^2 here. We used a simplified approach to calculate the FEs for gaseous products during pulsed CO_2RR, where we assumed that the CO_2RR-related currents equal the currents achieved upon equilibration. **Fig. S17** demonstrates that the time required for the current to equilibrate during a cathodic pulse is much smaller than the total pulse duration. Consequently, the current transferred due to additional electrochemical processes, which were not specifically accounted for, such as reductive or capacitive processes, is relatively small compared to the CO_2RR-related current. For the liquid products, ΔQ can be obtained by the integration of the cathodic current and subtraction of the charging current. More details about the calculations of all products can be found in our previous work.[1]

Supplementary Note 2. Validation of the machine learning approach

To extract the weights of the Cu and Zn species, conventional linear combination analysis (LCA) for the Cu K-edge was used, while for the Zn K-edge, the LCA fitting faced some limitations. First of all, as demonstrated in our previous study,[2] the Cu-Zn samples contain a Zn-oxide phase with a much higher degree of disorder and thus vary in structure from the wurtzite-type ZnO that was used as a reference. Further, alloy formation under reaction conditions can lead to a heterogenous mix of different Cu-Zn alloy structures (Cu-rich versus Zn-rich structures), while for our reference sample, the common $Cu_{70}Zn_{30}$ brass foil was used. To overcome these limitations, we developed a machine learning (ML) approach, which is described in more detail in a previous study.[2] This ML approach is based on the extraction of radial distribution functions of neighboring atoms from EXAFS data. In particular, a neural network (NN) is trained by using large sets of theoretically relevant structure models (oxide, fcc, and non-fcc phases) obtained from molecular dynamics (MD) and Monte Carlo (MC) simulations using empirical force field models. After validation of the NN with known structures (Zn, CuZn, and ZnO), we applied the NN to the EXAFS data of the operando measurements to extract the partial RDFs. The weight of different phases was obtained by integrating specific peaks of the partial RDFs divided by the true number of neighbors for the corresponding phase (oxide, fcc, or non-fcc). Compared to the LCA fitting, the NN-EXAFS analysis showed that a much higher contribution of an oxide phase remained in the sample even at -1.0 V. To verify those results, a conventional FEFFIT was applied to the data after 1 h of reduction, and a coordination number of 0.37 ± 0.26 was received (**Fig. S8**). This equals an oxide contribution of around 9 ± 6 %, which agrees with the results from the ML approach (ca. 12 %). Additionally, the LCA analysis (LCA2) was performed by using the spectrum collected under OCP as a reference instead of the wurtzite-type ZnO, which also resulted in higher amounts of this initial oxide structure (ca. 6 %) after 1 hour of reduction (**Fig. S5**). The trained NN could not be applied to the Zn K-edge XANES data set used for the cyclic voltammogram measurements in this study (**Fig. 4**) due to a glitch in the EXAFS spectra at 9878 eV (k-value: 7.5) of the QXAFS data collected at the ROCK beamline of the SOLEIL synchrotron. However, when performing the LCA fit on the QXAFS data from the initial reduction prior to the CV scan, the results for the weights of the species (Zn foil, CuZn foil, and wurtzite-tye ZnO) are much closer to those of the NN-EXAFS analysis performed for the data collected at the SuperXAS-X10DA beamline. Moreover, as already observed before, the general redox behavior of our sample remained the same and followed the same trends. Therefore, for the CV data set, only the conventional LCA was used for both edges (Cu and Zn K-edge) to follow the changes of species during the CV scans.
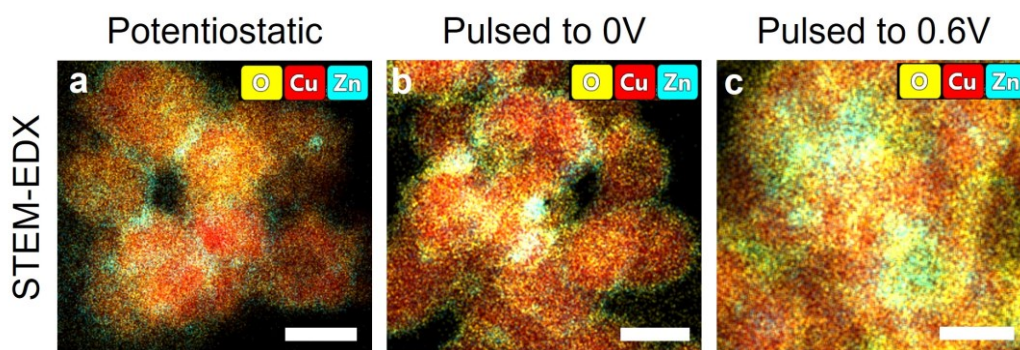
Supplementary Figures

Figure S1. STEM-EDX images of the Cu-Zn catalyst after different electrochemical treatments in CO_2-saturated 0.1 M $KHCO_3$. **a**, shows the catalyst after 1 h of potentiostatic CO_2RR at -1.0 V_{RHE}, **b**, after 1 h of pulsed CO_2RR with $E_a = 0$ V and **c**, after 1 h of pulsed CO_2RR with $E_a = 0.6$ V, where $E_c = -1.0$ V, $t_c = 4$ s and $t_a = 1$ s were fixed. The given scale bars correspond to 20 nm.
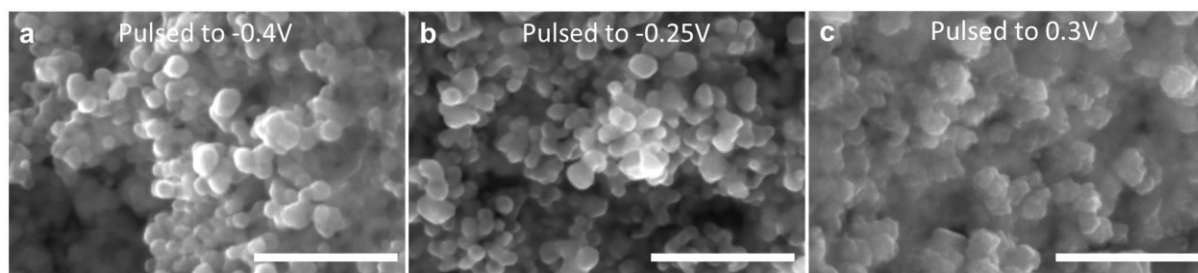

Figure S2. SEM images of Cu-Zn particles after different pulse protocols on carbon paper in CO_2-saturated 0.1 M $KHCO_3$. $E_c = -1.0$ V with $t_c = 4$ s and $t_a = 1$ s were fixed during pulsed CO_2RR for 1 h, while the anodic potential was varied in **a**, to $E_a = -0.4$ V, in **b**, to $E_a = -0.25$ V and in **c**, to $E_a = 0.3$ V. The scale bar corresponds to 300 nm.
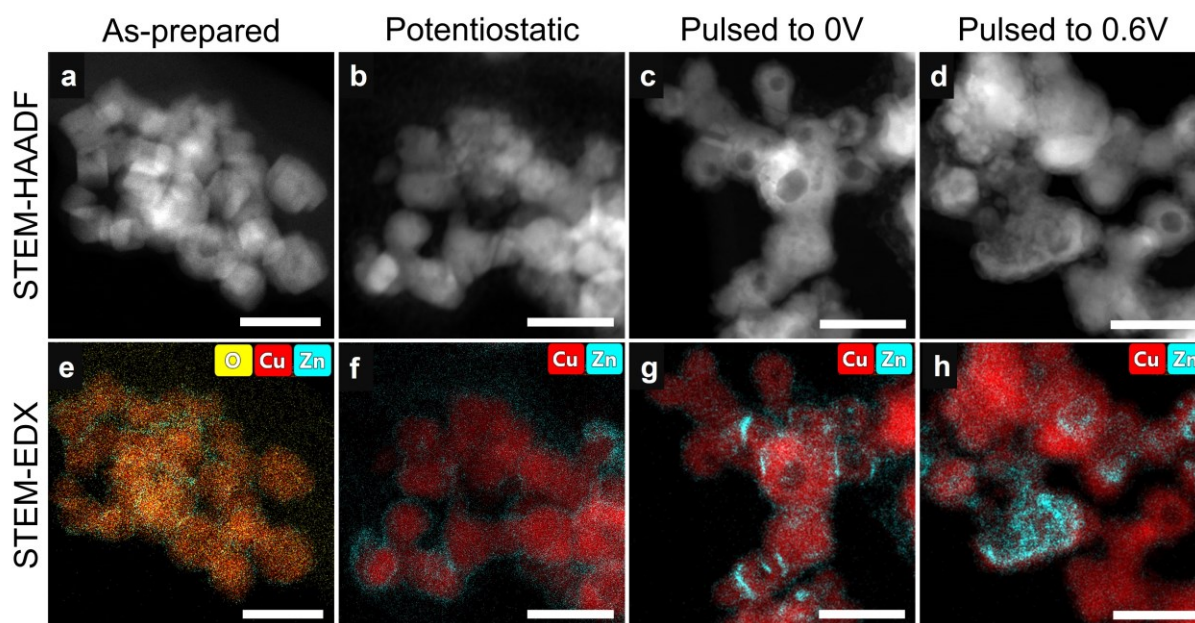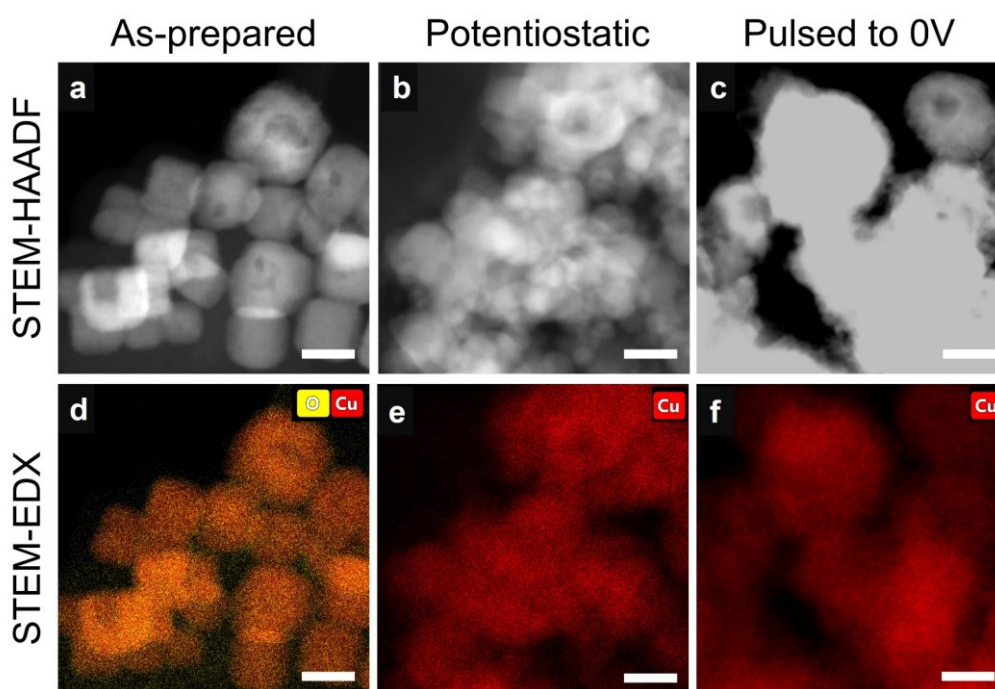
Figure S3. Additional STEM-HAADF and STEM-EDX images of the Cu-Zn catalyst after different conditions in the upper and lower panel, respectively. **a,e,** show the as-prepared state, **b,f,** after 1 h of potentiostatic CO_2RR at -1.0 V, **c,g,** after 1 h of pulsed CO_2RR with $E_a = 0$ V and **d,h,** after 1 h of pulsed CO_2RR with $E_a = 0.6$ V (fixed $E_c = -1.0$ V, $t_c = 4$ s and $t_a = 1$ s) in CO_2-saturated 0.1 M $KHCO_3$. The given scale bars correspond to 50 nm.

Figure S4. STEM-HAADF and STEM-EDX images of the bare Cu_2O cubes after different conditions in upper and lower panel, respectively. **a,d,** show the as-prepared state, **b,e,** after 1 h of potentiostatic CO_2RR at -1.0 V and **c,f,** after 1 h of pulsed CO_2RR with $E_a = 0$ V (fixed $E_c = -1.0$ V, $t_c = 4$ s and $t_a = 1$ s) in CO_2-saturated 0.1 M $KHCO_3$. The given scale bars correspond to 20 nm.
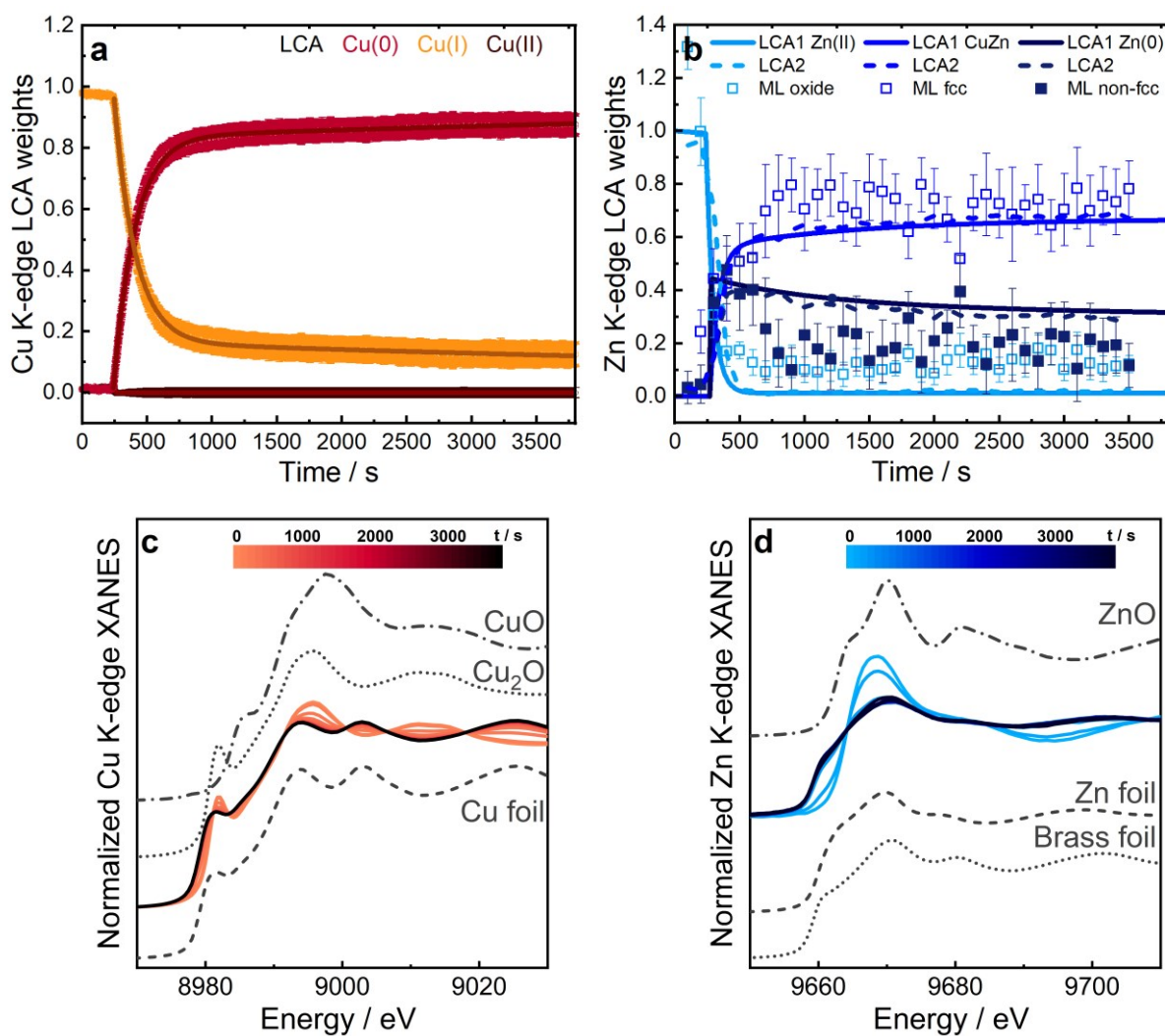
Figure S5. Evolution of XAS data of the Cu-Zn catalyst of Cu and Zn K-edges during the initial static CO$_2$RR for 1 h at -1.0 V in CO$_2$-saturated 0.1 M KHCO$_3$. **a**, Concentration of Cu(0), Cu(I) and Cu(II) species obtained by LCA of Cu K-edge and **b**, averaged concentration of Zn(0), Zn(II) and CuZn species obtained by LCA (LCA1 with standard references and LCA2 with oxide references from as-prepared state spectra) and concentrations of oxide, fcc-like and non-fcc-like phases obtained from ML-EXAFS analysis of Zn K-edge. **c,d**, show the averaged and normalized XANES spectra (100 spectra are averaged) of the Cu and Zn K-edge, respectively, with the corresponding references for both edges.
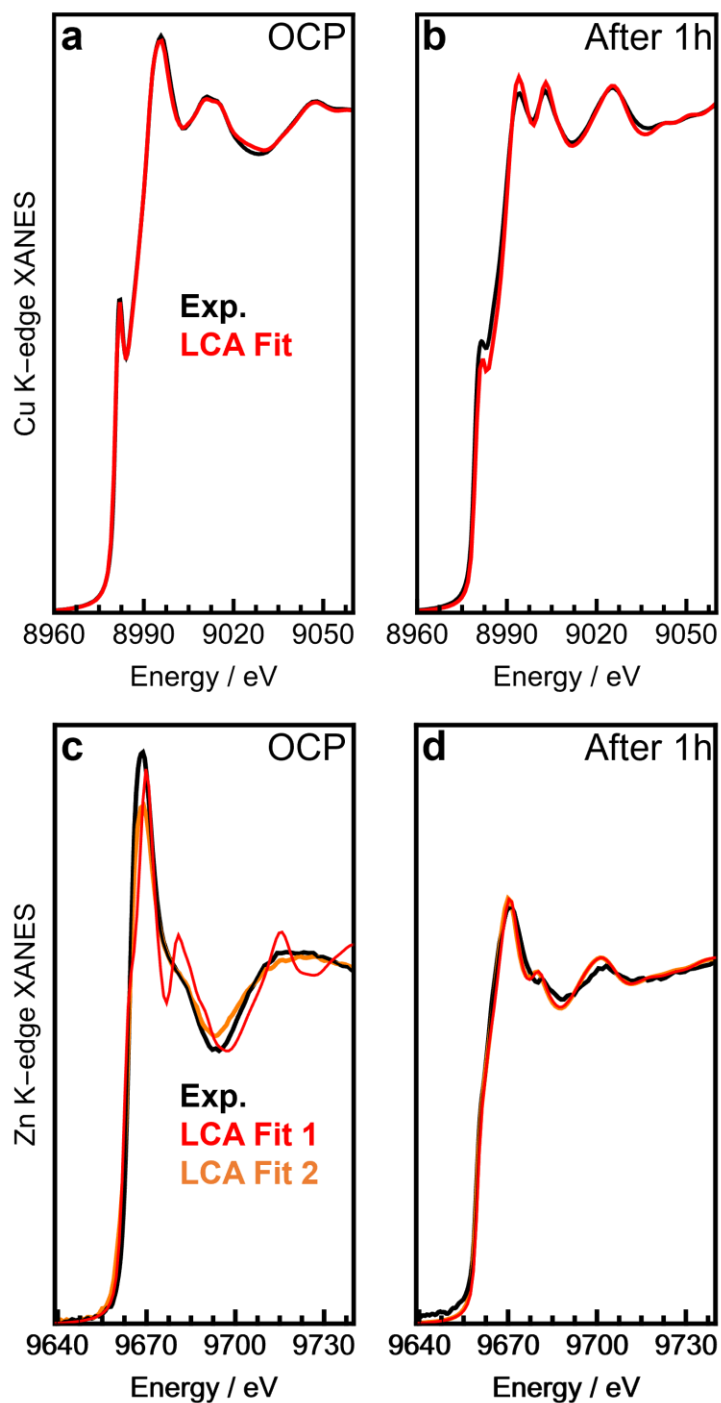
Figure S6. Exemplary LCA fits of the experimental XANES spectra. **a,b**, Cu K-edge under OCP and after 1 h of initial static CO_2RR at -1.0 V in CO_2-saturated 0.1 M $KHCO_3$, respectively. **c,d**, Zn K-edge under OCP and after 1 h of initial static CO_2RR at -1.0 V fitted with LCA1 (with standard references) and LCA2 (oxide reference equals as-prepared state spectra), respectively.
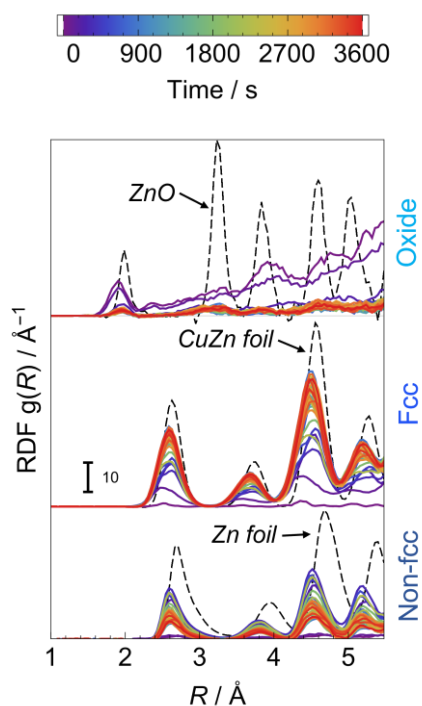
Figure S7. Time-dependent evolution of the radial distribution functions (RDFs) g(R) obtained by the NN-EXAFS analysis from operando Zn K-edge EXAFS data during initial static CO_2RR for 1 h at -1.0 V in CO_2-saturated 0.1 M $KHCO_3$. The partial RDFs correspond to an Zn oxide phase, a metallic phase with fcc-type structure and a metallic phase with non-fcc type structure. For clarity the RDFs are shifted vertically.
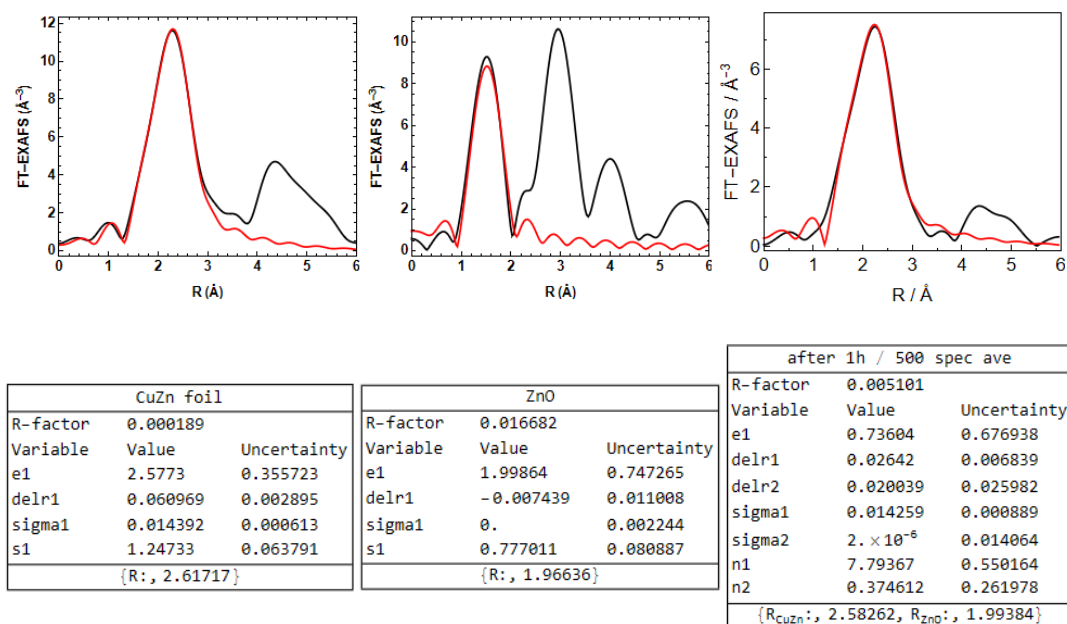

	CuZn foil	
R-factor	0.000189	
Variable	Value	Uncertainty
e1	2.5773	0.355723
delr1	0.060969	0.002895
sigma1	0.014392	0.000613
s1	1.24733	0.063791
{R:, 2.61717}		

	ZnO	
R-factor	0.016682	
Variable	Value	Uncertainty
e1	1.99864	0.747265
delr1	−0.007439	0.011008
sigma1	0.	0.002244
s1	0.777011	0.080887
{R:, 1.96636}		

after 1h / 500 spec ave		
R-factor	0.005101	
Variable	Value	Uncertainty
e1	0.73604	0.676938
delr1	0.02642	0.006839
delr2	0.020039	0.025982
sigma1	0.014259	0.000889
sigma2	$2. \times 10^{-6}$	0.014064
n1	7.79367	0.550164
n2	0.374612	0.261978
{R_{CuZn}:, 2.58262, R_{ZnO}:, 1.99384}		

Figure S8. NN-EXAFS analysis results were verified by applying a conventional FEFFIT to the data after 1 h of at -1.0 V in CO_2-saturated 0.1 M $KHCO_3$, where a coordination number of 0.37(26) for the oxide species (equals a fraction of 9(6) %) was obtained in agreement with the results from the ML approach.
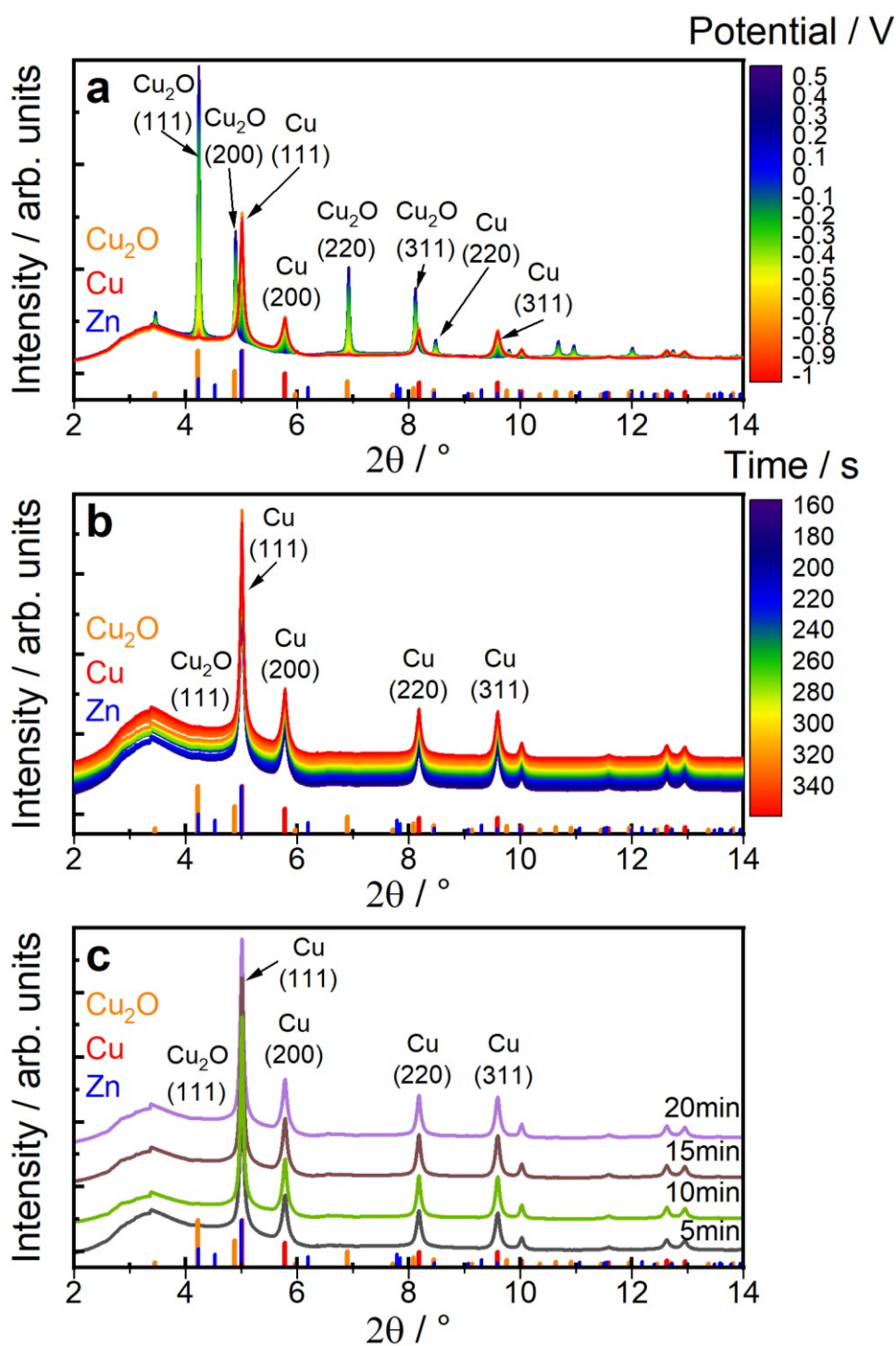
Figure S9. HE-XRD pattern of the Cu-Zn catalyst during static CO_2RR conditions with reference peaks of Cu_2O, Cu, and Zn. **a**, Averaged XRD patterns during LSV scan from OCP to -1.0 V with a scan rate of 10 mV s^{-1} in CO_2-saturated 0.1 M $KHCO_3$. **b**, Averaged XRD patterns during the first five minutes at -1.0 V with an offset of the diffractograms for better visibility of changes. **c**, XRD pattern at 5, 10, 15, and 20 minutes at -1.0 V (with a time resolution of 5 s/diffractogram). The XRD patterns correspond to the average of 5 XRD patterns, acquired with 0.2 s/diffractogram, that can be translated into a time resolution of 1 s/diffractogram shown here.
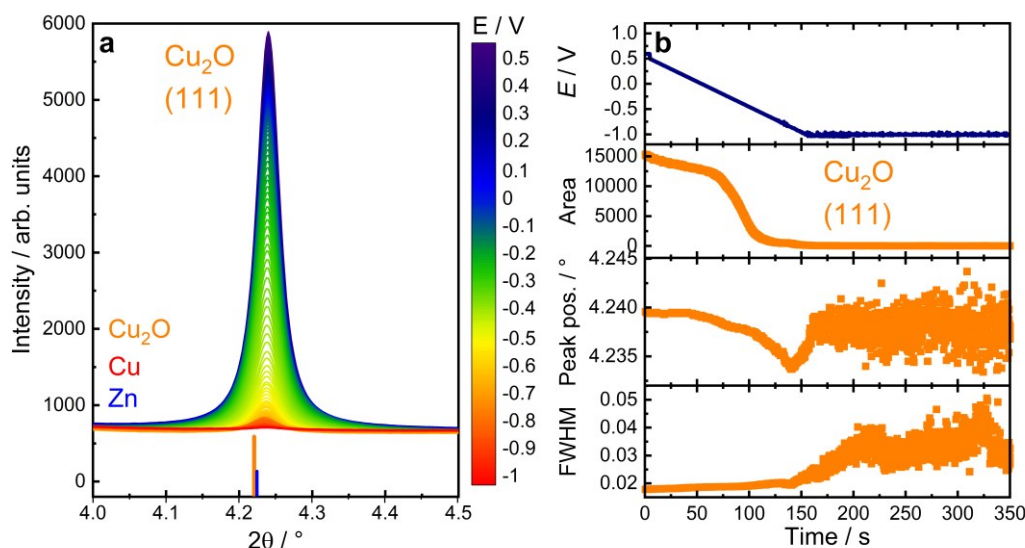
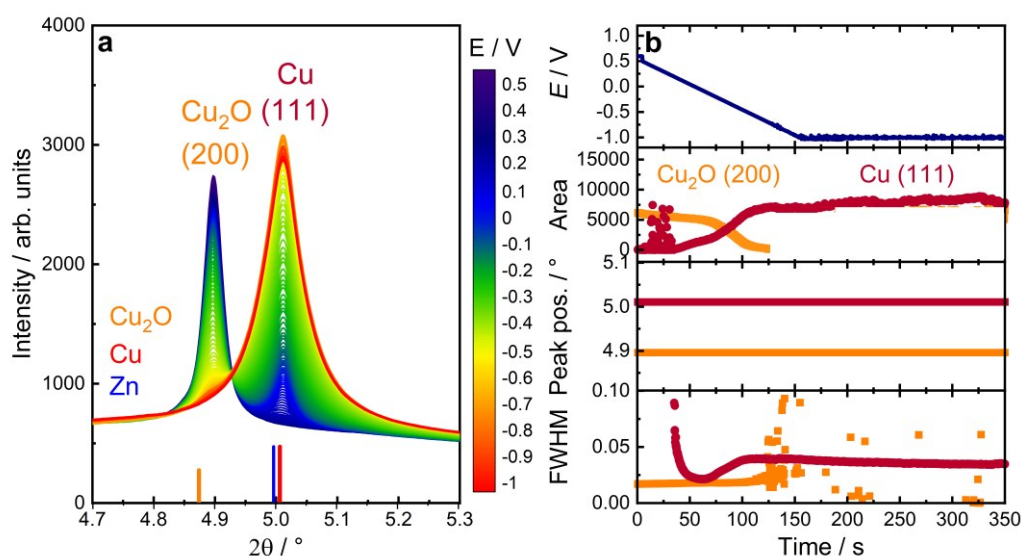**Figure S10.** Extract of HE-XRD patterns of $Cu_2O(111)$ and corresponding fits of Cu-Zn catalyst during LSV and static CO_2RR conditions. **a**, Extract of averaged XRD pattern during the LSV scan from OCP to -1.0 V with a scan rate of 10 mV s^{-1} in CO_2-saturated 0.1 M KHCO$_3$. **b**, Area (second row), peak position (third row), and FWHM (fourth row) extracted from fits of $Cu_2O(111)$ with respect to the applied potential (top row). The XRD patterns correspond to the average of 5 XRD patterns, acquired with 0.2 s/diffractogram, that can be translated into a time resolution of 1 s/diffractogram shown here.

Figure S11. Extract of HE-XRD pattern of $Cu_2O(200)$ and $Cu(111)$ and corresponding fits of Cu-Zn catalyst during LSV and static CO_2RR conditions. **a**, Extract of averaged XRD pattern during the LSV scan from OCP to -1.0 V with a scan rate of 10 mV s^{-1} in CO_2-saturated 0.1 M KHCO$_3$. **b**, Area (second row), peak position (third row), and FWHM (fourth row) extracted from fits of $Cu_2O(200)$ and $Cu(111)$ with respect to the applied potential (top row). The XRD patterns correspond to the average of 5 XRD patterns, acquired with 0.2 s/diffractogram, that can be translated into a time resolution of 1 s/diffractogram shown here.
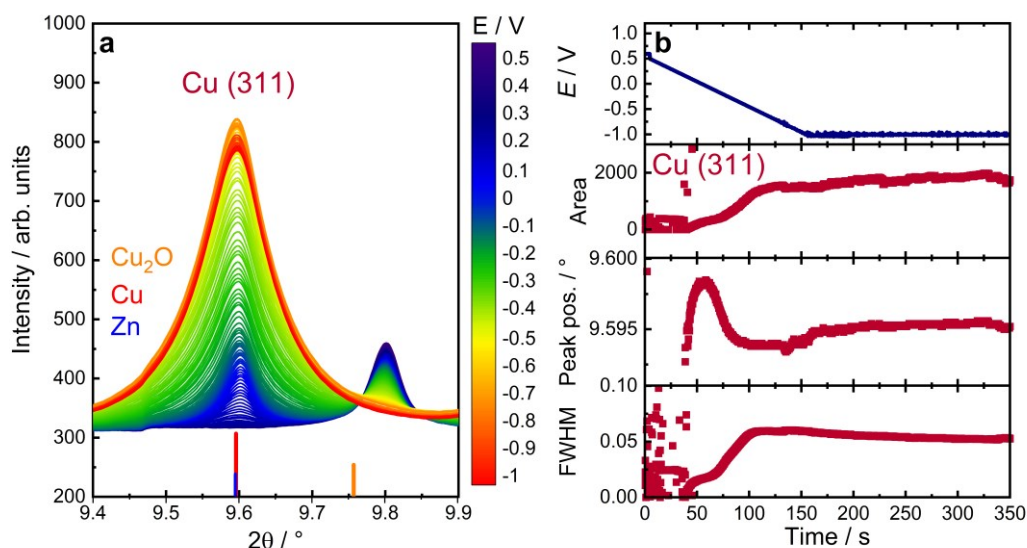
Figure S12. Extract of HE-XRD pattern of Cu(311) and corresponding fits of the Cu-Zn catalyst during LSV and static CO_2RR conditions. **a**, Extract of averaged XRD patterns during the LSV scan from OCP to -1.0 V with a scan rate of 10 mV s^{-1} in CO_2-saturated 0.1 M $KHCO_3$. **b**, Area (second row), peak position (third row), and FWHM (fourth row) extracted from fits of Cu(311) with respect to the applied potential (top row). The XRD patterns correspond to the average of 5 XRD patterns, acquired with 0.2 s/diffractogram, that can be translated into a time resolution of 1 s/diffractogram shown here.
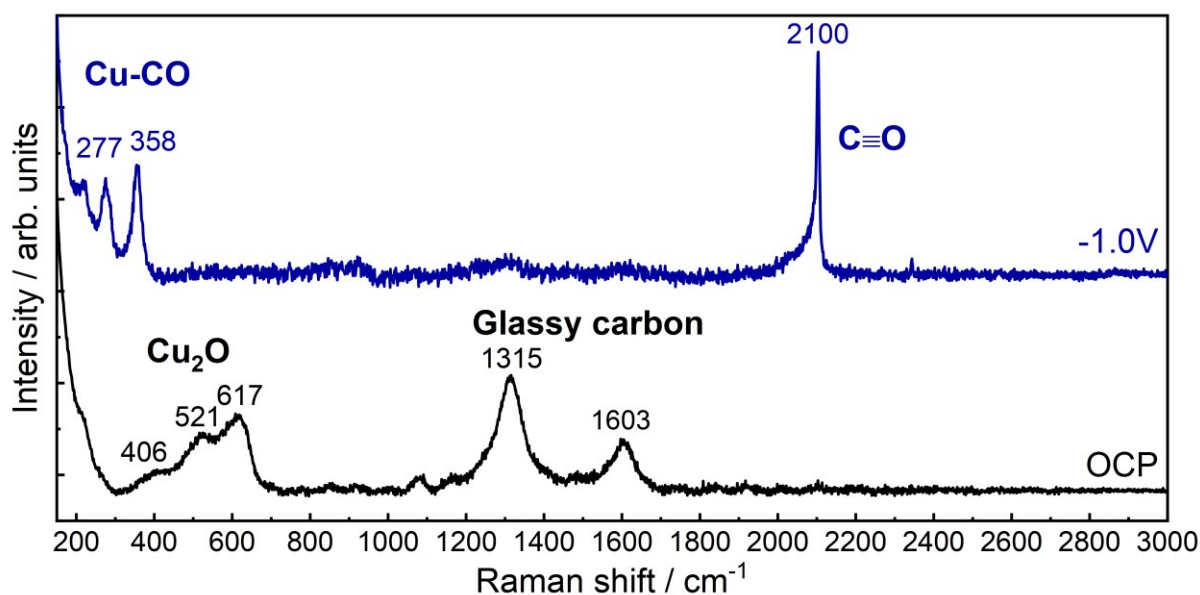
Figure S13. Operando SERS spectra of the Cu-Zn catalyst at OCP and during static CO_2RR for 1 h at -1.0 V in CO_2-saturated 0.1 M $KHCO_3$. The peaks at 1005 and 1072 cm^{-1} can be assigned to the vibrations of HCO_3^- and CO_3^{2-} in aqueous solution, respectively, and the peaks at 1313 and 1600 cm^{-1} correspond to the glassy carbon support.[3, 4] No peaks were detected in the C-H vibration region from 2700 to 3000 cm^{-1}. We note that the spectrum under OCP condition was recorded with a high laser power of 25 mW, while the power was decreased to 2.5 mW for the spectrum at -1.0 V to obtain appropriate signal intensities. This is a result of the strong SERS effect of the plasmonic metallic Cu nanoparticles that are formed at -1.0 V. The higher power under OCP conditions increases the laser penetration depth, which may strengthen the signals from the glassy carbon support. The HCO_3^- and CO_3^{2-} bands are small at -1.0 V due to the higher coverage of the catalyst surface with CO and other intermediates.
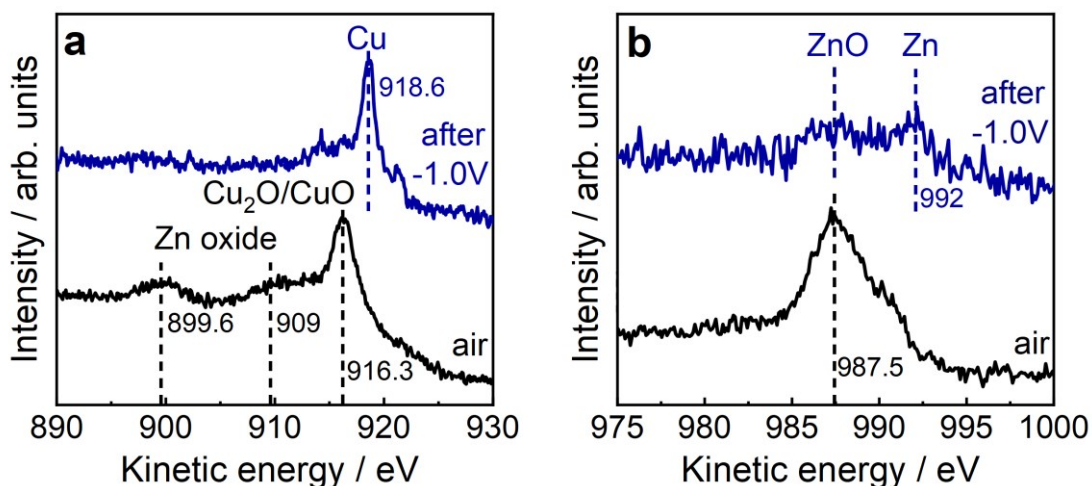
Figure S14. Quasi-in situ Auger spectra of the Cu-Zn catalyst in air and after 1 h of static CO_2RR at -1.0 V (without air exposure) in CO_2-saturated 0.1 M $KHCO_3$. **a**, Cu LMM and **b**, Zn LMM with corresponding assignment.
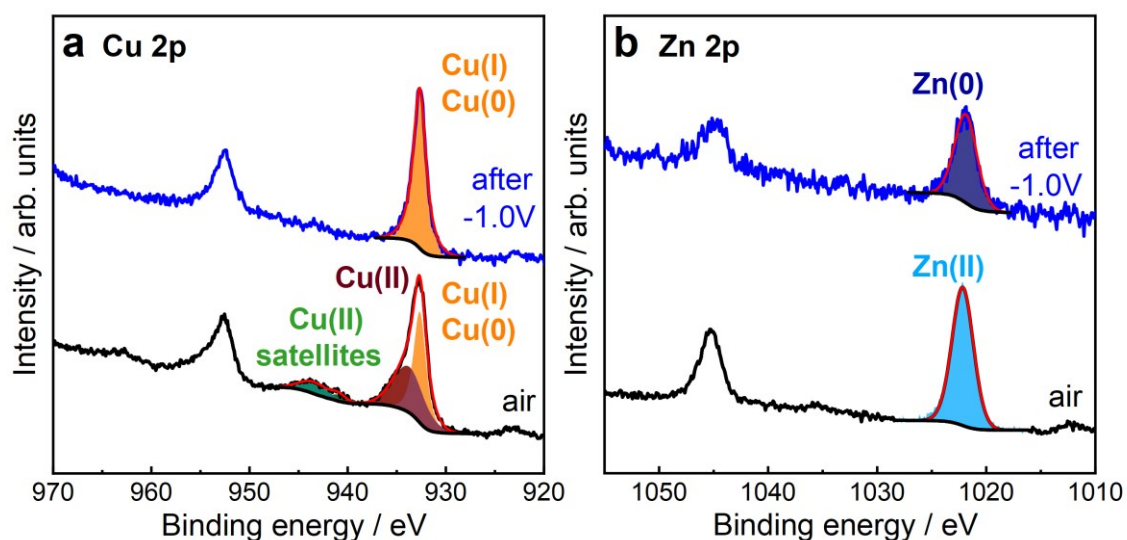

Figure S15. Quasi-in situ core level regions of the Cu-Zn catalyst in the as-prepared state (corresponds to the state in air) and after 1 h of static CO_2RR at -1.0 V (without air exposure) in CO_2-saturated 0.1 M $KHCO_3$. **a**, Cu 2p region and **b**, Zn 2p region with corresponding fits (red line). The Cu 2p core level region of the as-prepared sample shows the presence of Cu(0)/Cu(I) and a shake-up satellite corresponding to Cu(II).
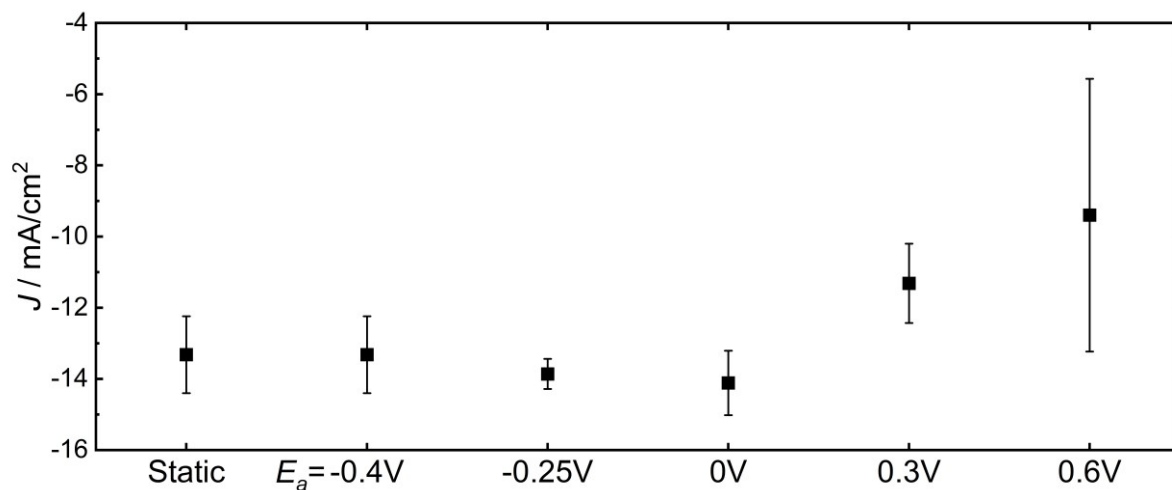
Figure S16. Averaged current densities, J, of the Cu-Zn catalyst under potentiostatic conditions (-1.0 V) and under pulsed electrolysis conditions with a fixed E_c value at -1.0 V and different E_a values and t_c = 4 s and t_a = 1 s during 1 h of the reaction in CO_2-saturated 0.1 M $KHCO_3$. The large error bar at E_a = 0.6 V highlights the instability of the current density, which increased significantly during the reaction under these conditions.
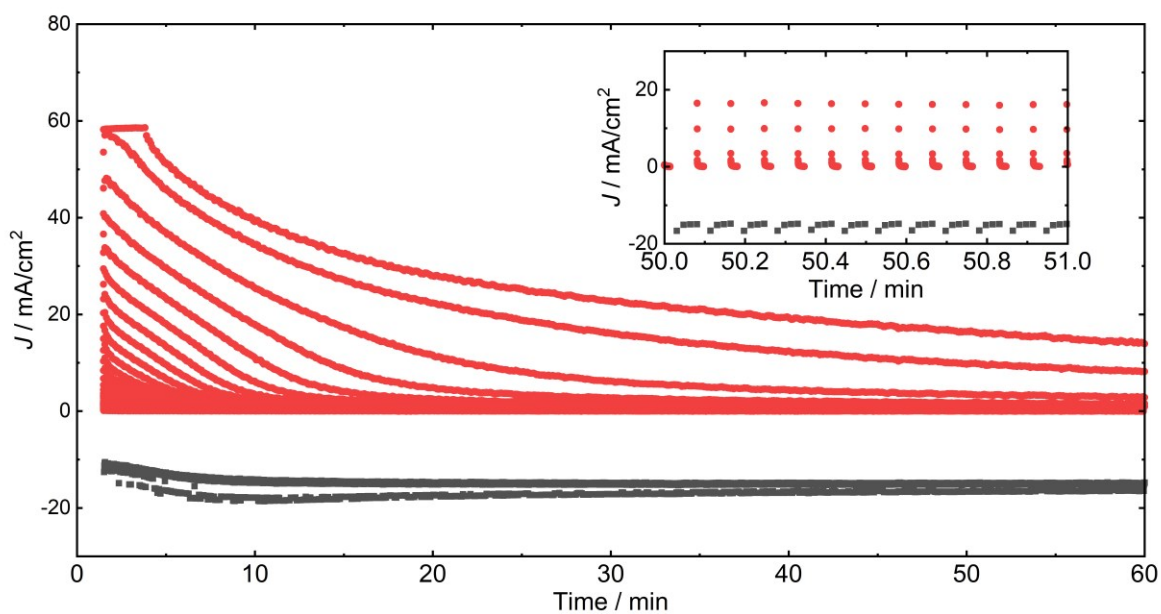

Figure S17. Temporal evolution of the current density J of the Cu-Zn catalyst under pulsed electrolysis with E_c = -1.0 V, E_a = 0 V, and t_c = 4 s, and t_a = 1 s during 1 h of reaction in CO_2-saturated 0.1 M $KHCO_3$.
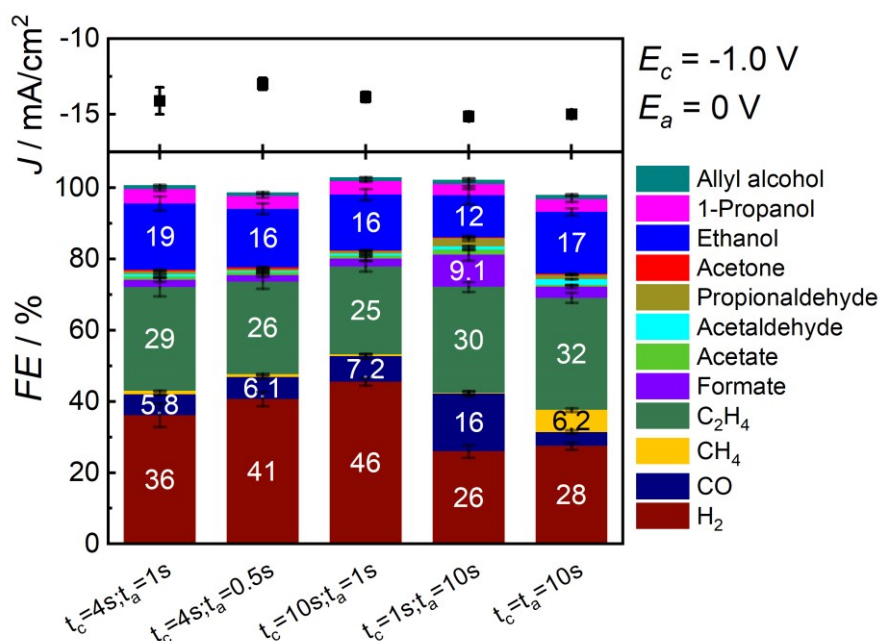
Figure S18. Averaged current densities (top) and Faradaic efficiencies (bottom) of the Cu-Zn catalyst under pulsed electrolysis conditions with a fixed cathodic potential E_c and anodic potential E_a values at -1.0 V and 0 V, respectively, and varied cathodic and anodic time lengths t_c and t_a during 1 h of reaction in CO_2-saturated 0.1 M $KHCO_3$.
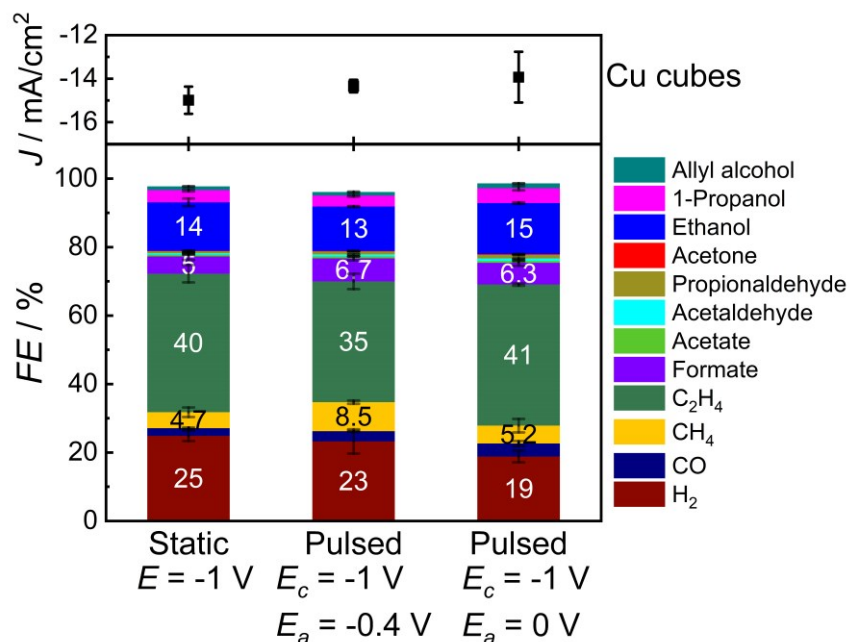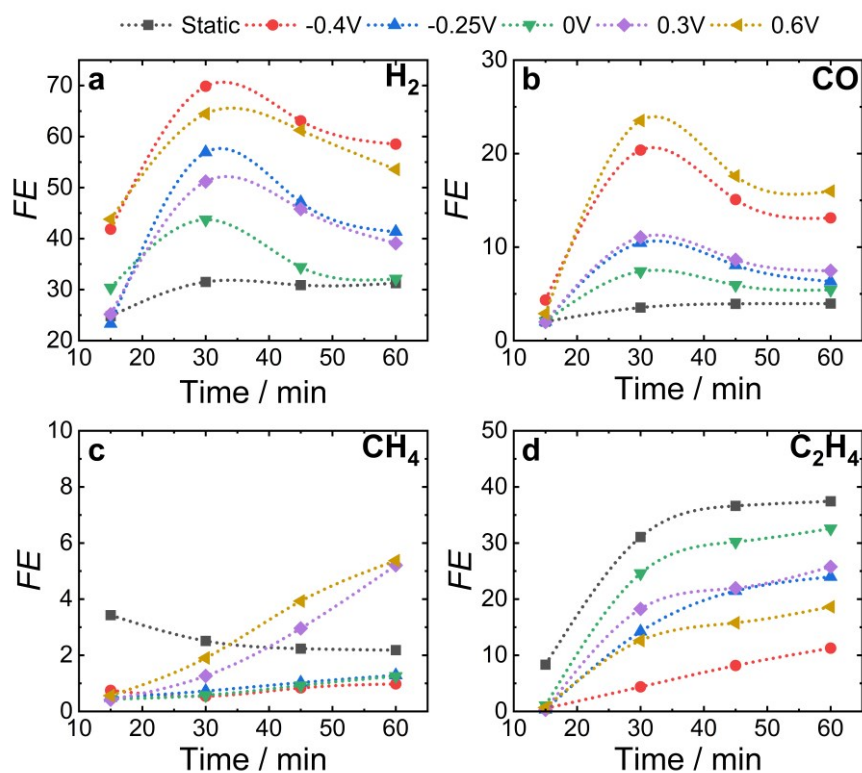

Figure S19. Averaged current densities (top) and Faradaic efficiencies (bottom) of Cu cubes as reference catalyst under static CO_2RR at -1.0 V and under pulsed electrolysis conditions with E_c = -1.0 V, E_a = 0 V, t_c = 4 s and t_a = 1 s during 1 h of reaction in CO_2-saturated 0.1 M $KHCO_3$.

Figure S20. Evolution of the selectivities of the gaseous products during pulsed CO_2RR with E_c = -1.0 V, E_a = 0 V, t_c = 4 s, and t_a = 1 s for 1 h of the pre-reduced Cu-Zn catalyst in CO_2-saturated 0.1 M $KHCO_3$. **a**, shows the Faradaic efficiency of hydrogen, **b**, carbon monoxide, **c**, methane, and **d**, ethylene.
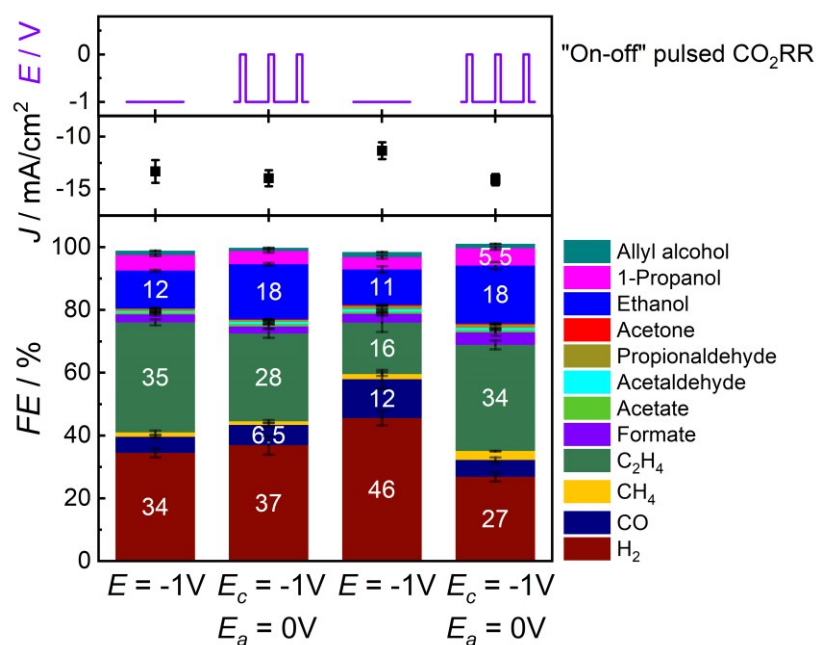

Figure S21. Schematic potential sequences (top), averaged current densities (middle), and Faradaic efficiencies (bottom) of the Cu-Zn catalyst under sequentially changing static CO_2RR at -1.0 V for 1 h each time followed by pulsed CO_2RR with E_c = -1.0 V, E_a = 0 V, t_c = 4 s and t_a = 1 s for 2 h each time in CO_2-saturated 0.1 M $KHCO_3$. Changes in the FEs were paralleled by a decrease in current density.
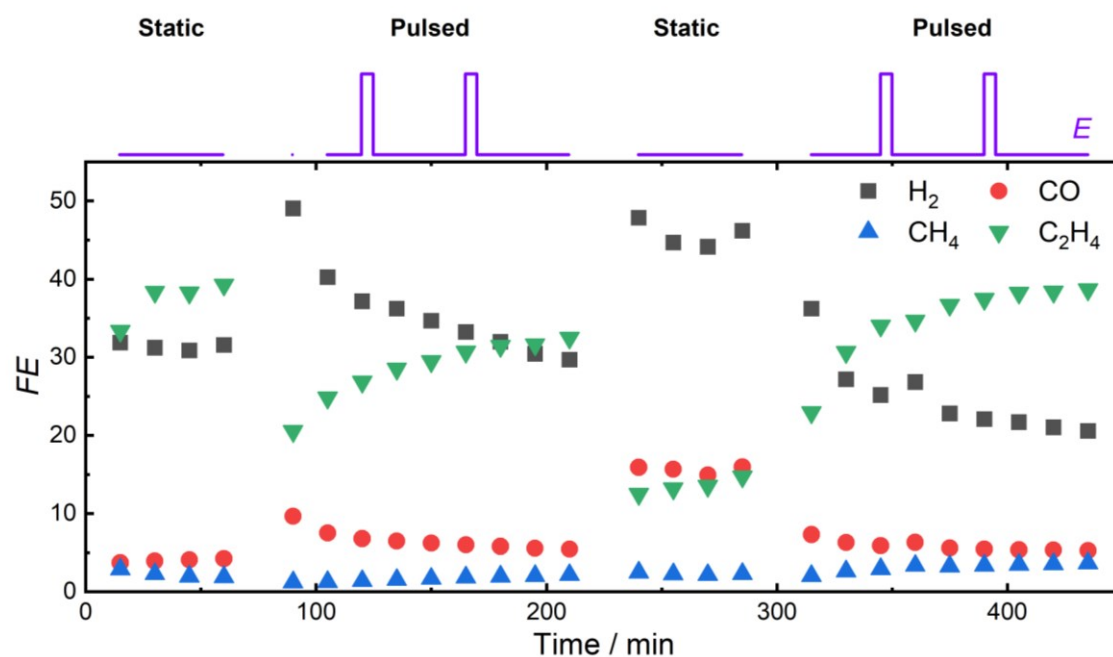
15

Figure S22. Temporal evolution of the selectivities of the gaseous products during static CO_2RR for 1 h and pulsed CO_2RR with E_c = -1.0 V, E_a = 0 V, t_c = 4 s, and t_a = 1 s for 2 h of the Cu-Zn catalyst in CO_2-saturated 0.1 M KHCO$_3$. The reaction time was set to 2 h of pulsed CO_2RR to ensure a stabilized selectivity evolution due to the activation time of the catalyst. The gaseous products here are hydrogen, carbon monoxide, methane, and ethylene. Potential pulses are shown schematically. Interestingly, the time-dependent evolution of the gaseous products indicates an activation time for the C$_{2+}$ product formation of ~30 min after each (re-)started pulsed CO_2RR experiment.
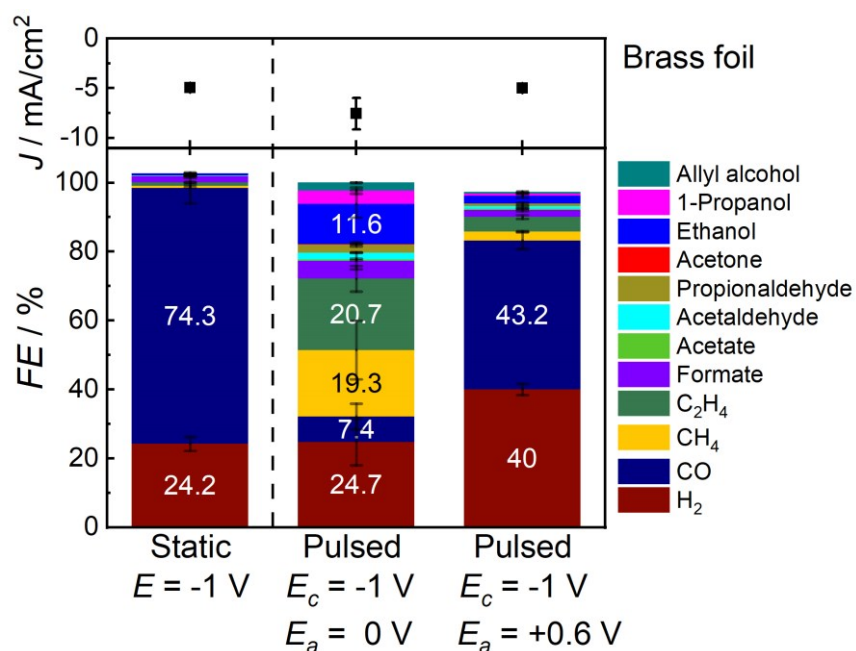

Figure S23. Averaged current densities (top) and Faradaic efficiencies (bottom) of a CuZn bulk brass foil as reference catalyst under static CO_2RR at -1.0 V and under pulsed CO_2RR with E_c = -1.0 V and E_a = 0 V or 0.6 V, and t_c = 4 s and t_a = 1 s during 1 h of reaction in CO_2-saturated 0.1 M KHCO$_3$.
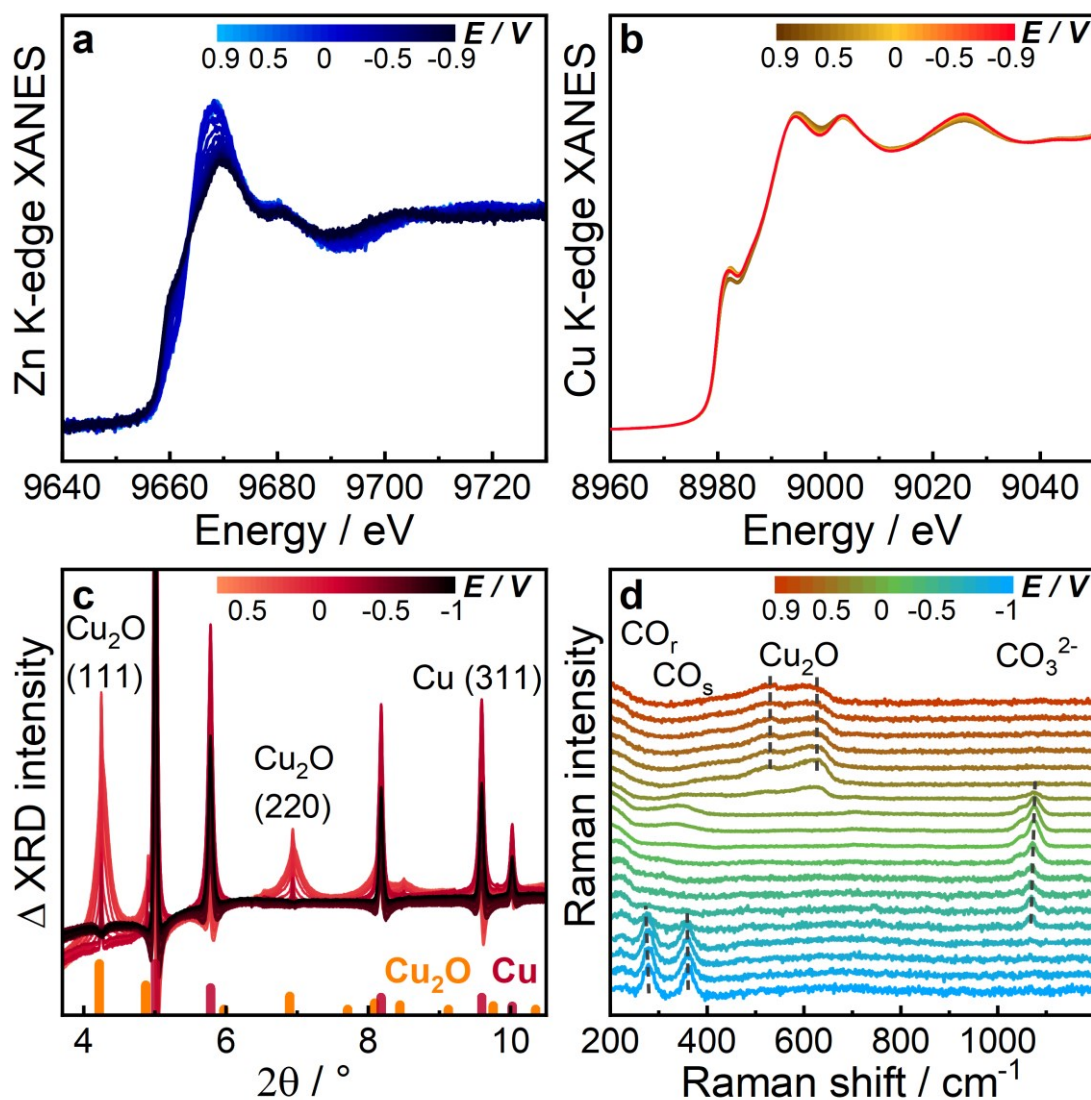
16

Figure S24. Averaged spectra and diffractograms during the cathodic scan of a CV voltammogram. **a,b**, XANES spectra of Zn K-edge and Cu K-edge, respectively, during from 0.9 to -0.9 V. **c**, Averaged Δ HE-XRD patterns (after subtraction of the XRD pattern acquired during static CO_2RR at -1.0 V before CV) from -0.7 to -1.0 V. **d**, Averaged SERS spectra obtained while changing the potential from 0.9 to -1.0 V. The Cu-Zn sample was pre-reduced for 1 h at -1.0 V under CO_2RR conditions before the CV in CO_2-saturated 0.1 M $KHCO_3$.
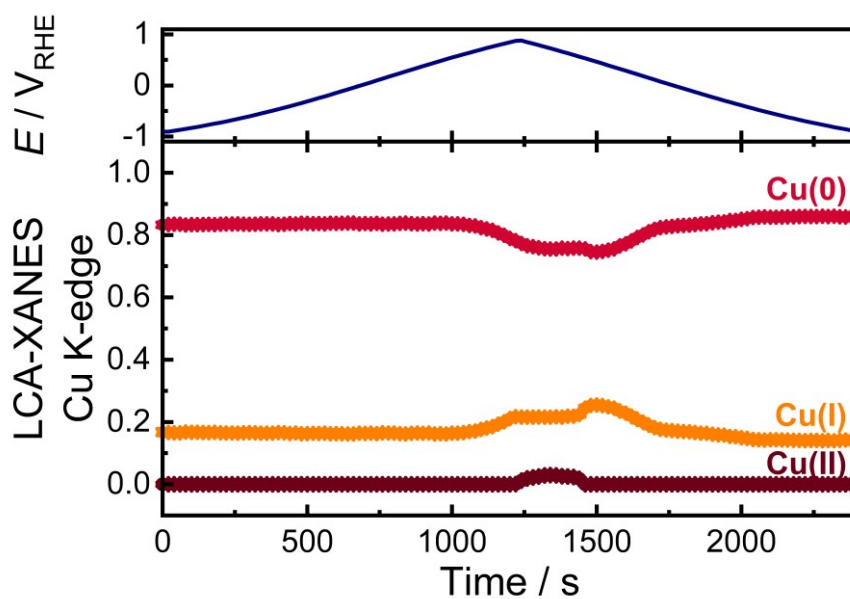
Figure S25. LCA-XANES analysis results of Cu K-edge of pre-reduced Cu-Zn catalyst during a CV scan from -0.9 V → 0.9 V → -0.9 V in CO_2-saturated 0.1 M $KHCO_3$ with corresponding applied potential.
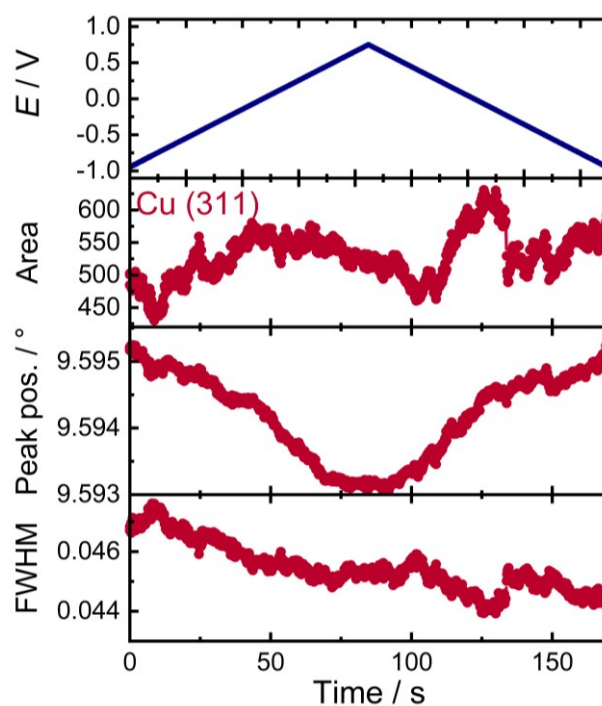
Figure S26. Fits of HE-XRD patterns of Cu(311) of the Cu-Zn catalyst during CV from -1.0 V → 0.7 V → -1.0 V in CO_2-saturated 0.1 M $KHCO_3$. Area (second row), peak position (third row) and FWHM (fourth row) extracted from fits of Cu(311) with respect to the applied potential (top row).
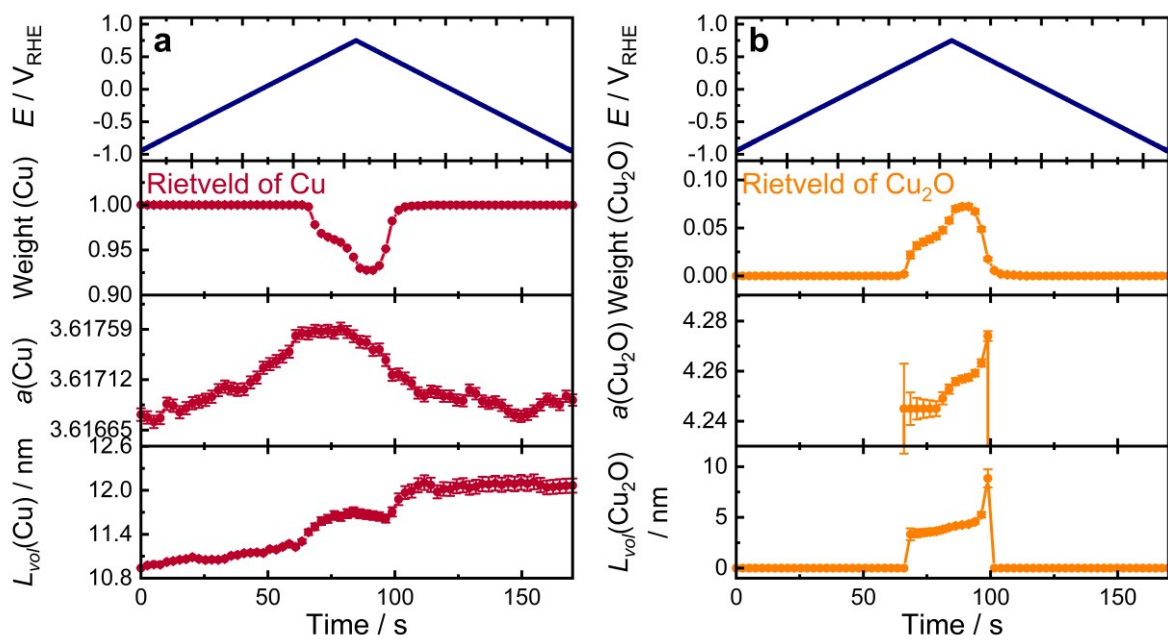
Figure S27. Rietveld analysis of HE-XRD pattern of **a**, Cu and **b**, Cu_2O of the Cu-Zn catalyst during a CV from -1.0 V → 0.7 V → -1.0 V in CO_2-saturated 0.1 M $KHCO_3$. Weight (second row), lattice parameter a (third row) and coherence length L_{vol} (fourth row) in respect to the applied potential (top row).
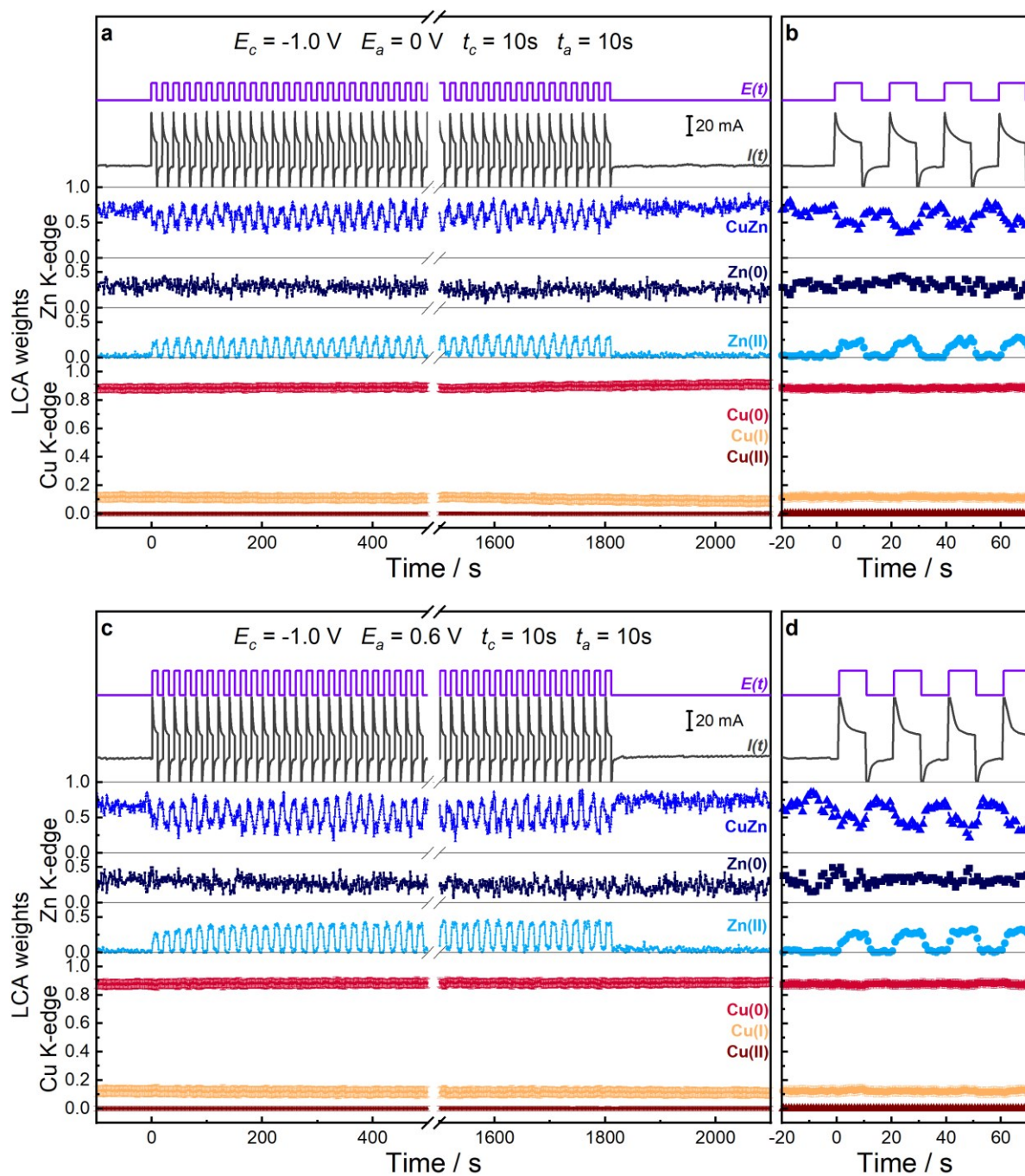
Figure S28. LCA-XANES analysis results of the Zn and Cu K-edges of pre-reduced Cu-Zn catalyst during pulsed CO_2RR with $t_c = t_a = 10$ s in CO_2-saturated 0.1 M $KHCO_3$. E_c is constant at -1.0 V, while **a,b**, are at $E_a = 0$ V and **c,d**, are at $E_a = 0.6$ V. **b,d**, show an extract of the full-time pulsed CO_2RR for better visibility.

Figure S29. LCA-XANES analysis results of the Zn and Cu K-edges of pre-reduced Cu-Zn catalyst during pulsed CO_2RR with t_c = 4 s and t_a = 1 s in CO_2-saturated 0.1 M $KHCO_3$. E_c is constant at -1.0 V, while **a,b**, are at E_a = 0 V and **c,d**, are at E_a = 0.6 V. **b,d**, show an extract of the full-time pulsed CO_2RR for better visibility.
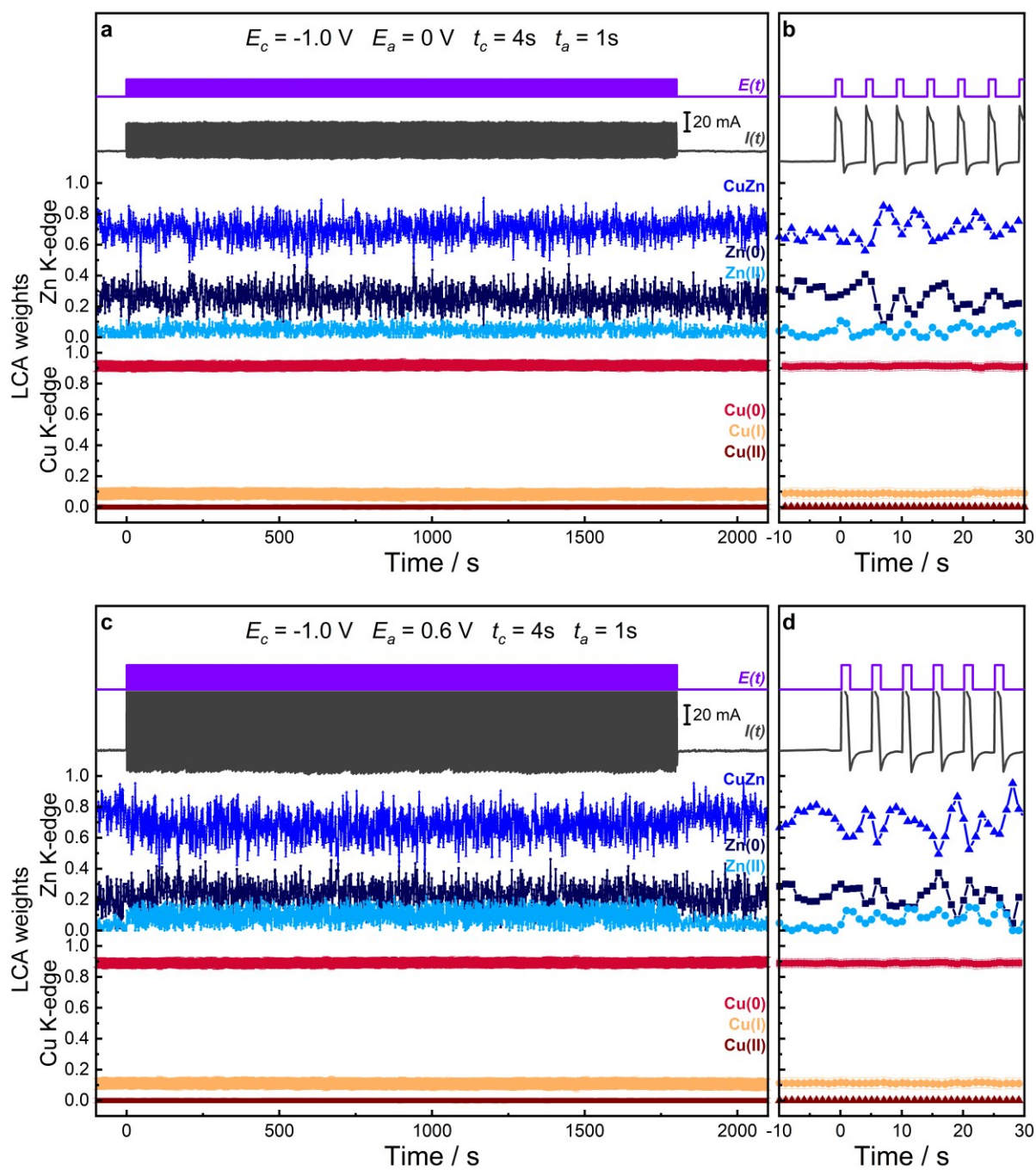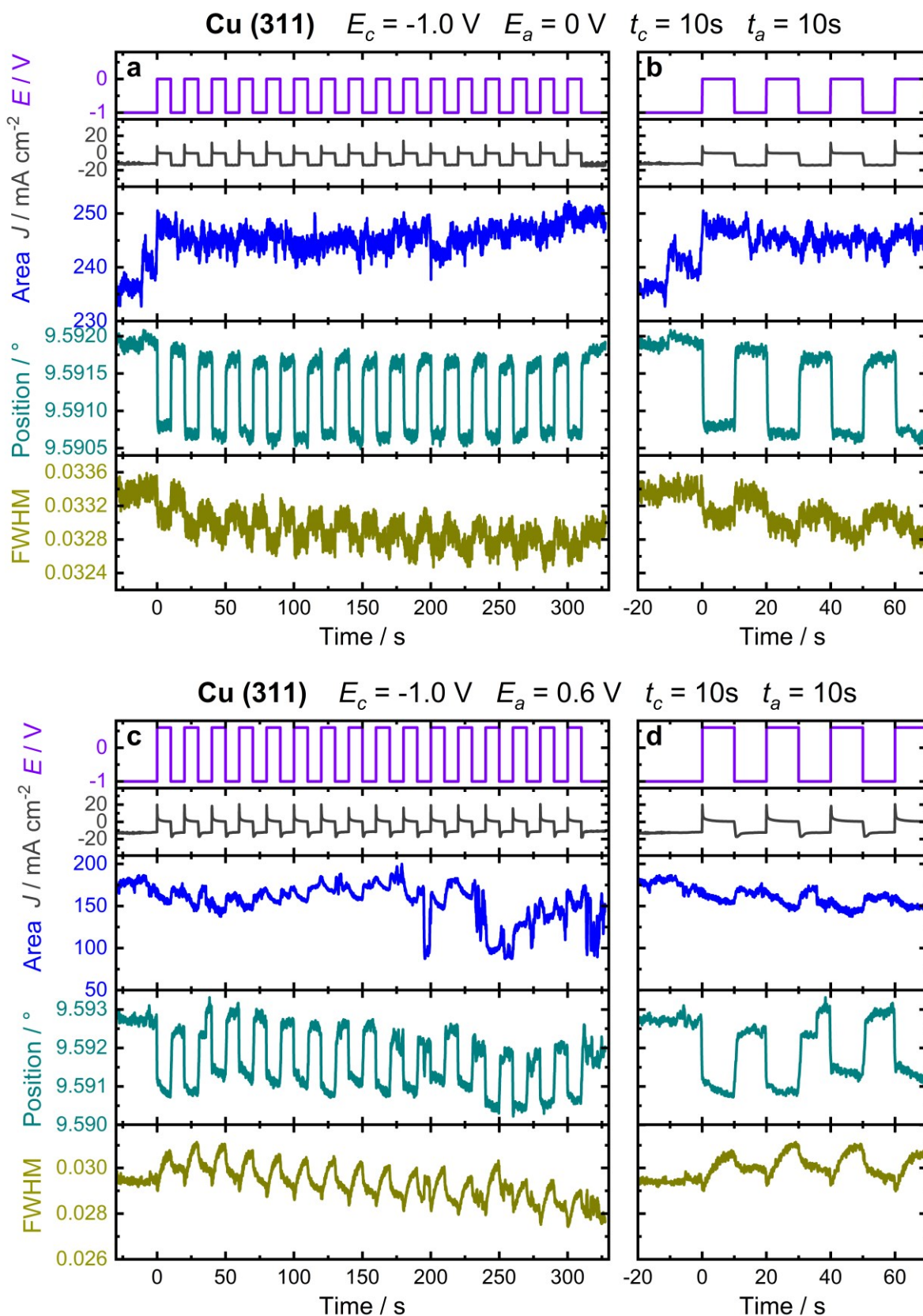
Figure S30. Temporal evolution of the area, peak position, and FWHM extracted from the fits of Cu(311) of HE-XRD patterns with respect to the applied potential and current density (top) during pulsed CO_2RR with $t_c = t_a = 10$ s in CO_2-saturated 0.1 M $KHCO_3$. E_c is constant at -1.0 V, while **a,b,** are at $E_a = 0$ V and **c,d,** are at $E_a = 0.6$ V. **b,d,** show an extract of the full-time pulsed CO_2RR for better visibility.
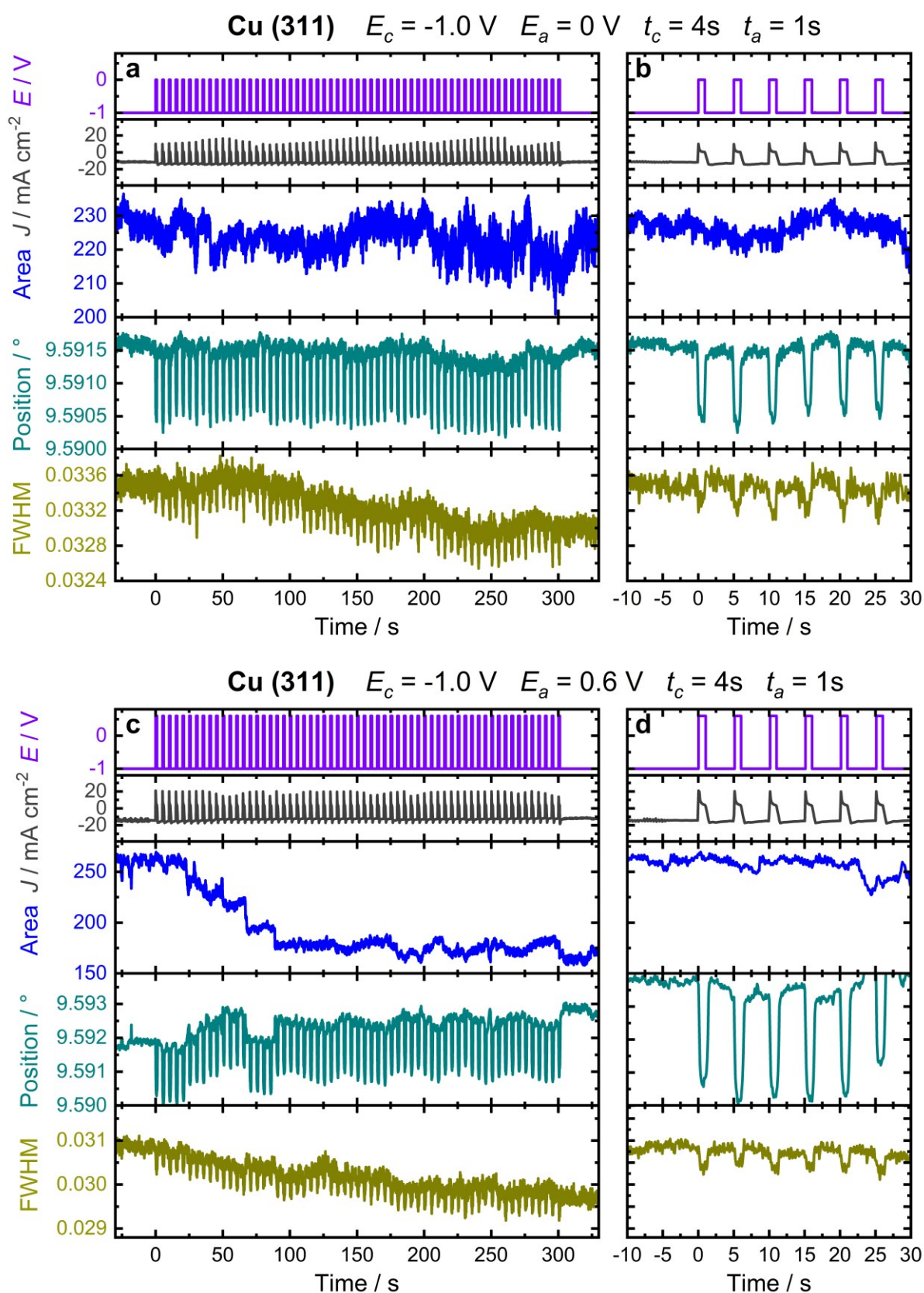
Figure S31. Temporal evolution of the area, peak position, and FWHM extracted from the fits of Cu(311) of the HE-XRD patterns with respect to the applied potential and current density (top) during pulsed CO_2RR with $t_c = 4$ s and $t_a = 1$ s in CO_2-saturated 0.1 M $KHCO_3$. E_c is constant at -1.0 V, while **a,b**, are at $E_a = 0$ V and **c,d**, are at $E_a = 0.6$ V. **b,d**, show an extract of the full-time pulsed CO_2RR for better visibility.
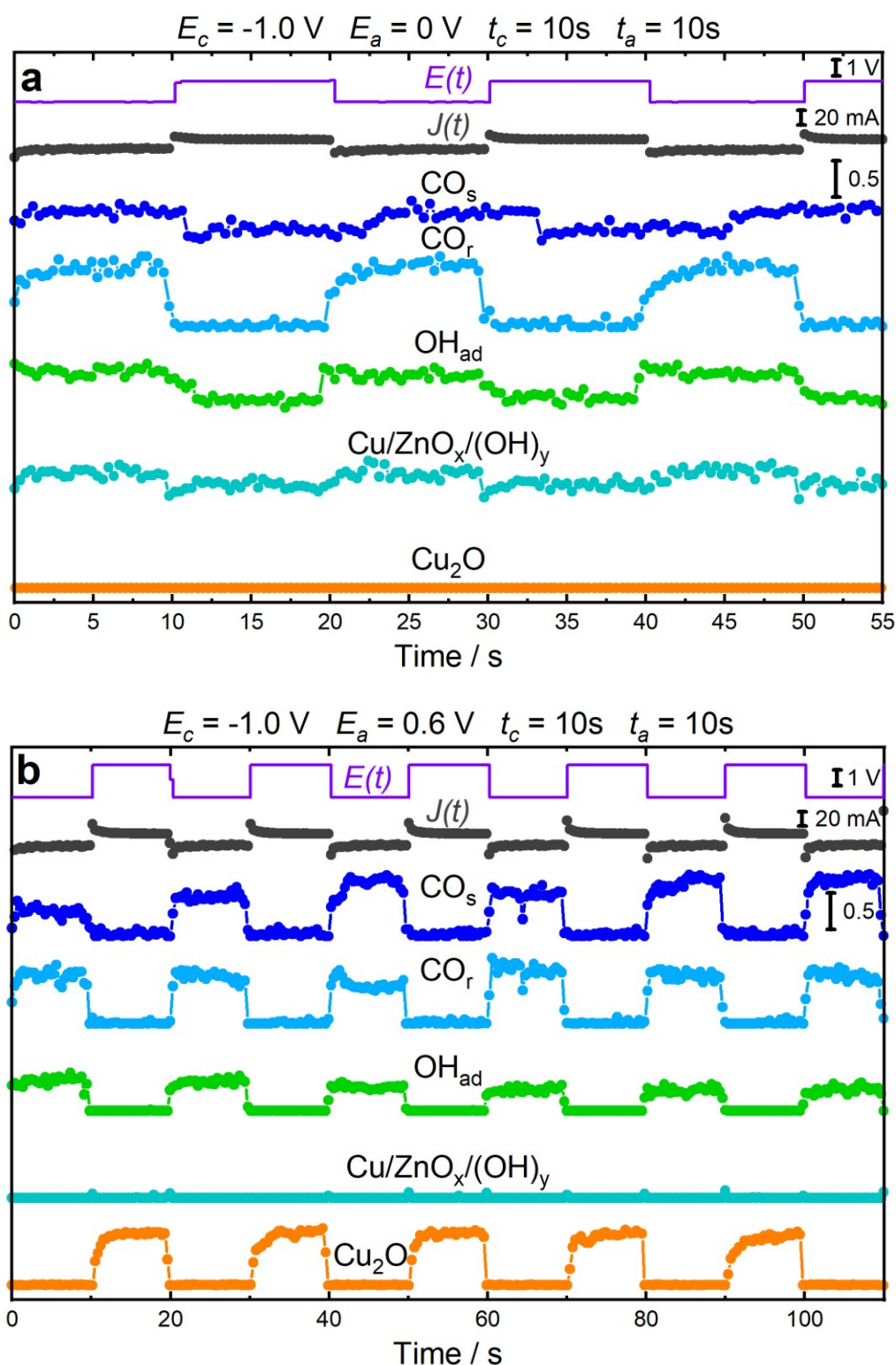
Figure S32. Temporal evolution of the chemical state and adsorbate coverage as Cu-CO stretching (CO_s, 360 cm^{-1}) and rotation (CO_r, 280 cm^{-1}) vibrations, OH_{ad} vibration on Cu (490 cm^{-1}), $Cu/ZnO_x/(OH)_y$ species (370 cm^{-1}) and Cu_2O species (405, 530, 610 cm^{-1}) obtained by fitting the intensities of the bands from the SERS spectra with respect to the applied potential and current density (top) during pulsed CO_2RR in CO_2-saturated 0.1 M $KHCO_3$ with $t_c = t_a = 10$ s. E_c is constant at -1.0 V, while **a,b,** are at E_a = 0 V and **c,d,** are at E_a = 0.6 V. **b,d,** show an extract of the full-time pulsed CO_2RR for better visibility.
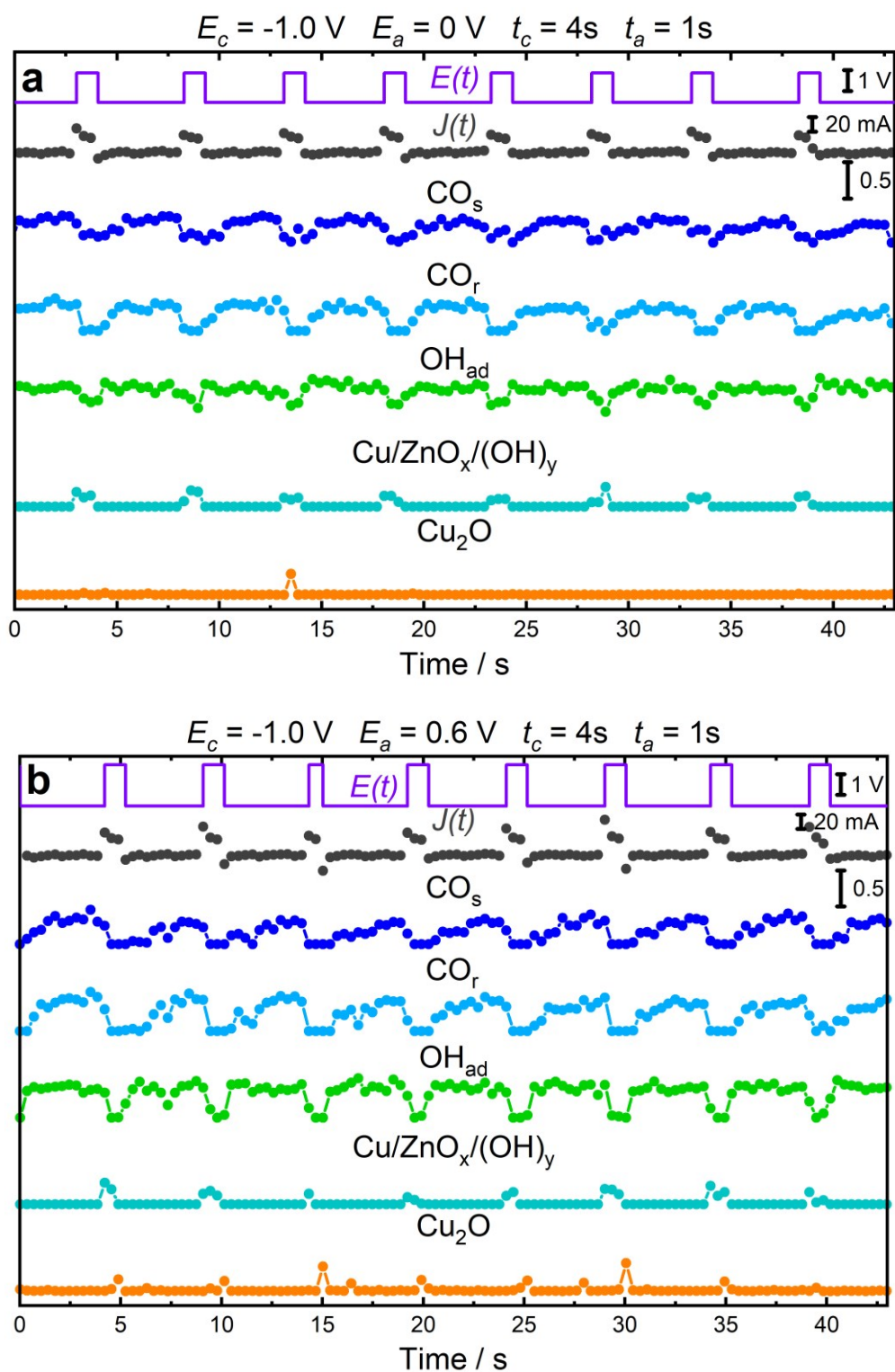
Figure S33. Temporal evolution of the chemical state and adsorbate coverage as Cu-CO stretching (CO_s, 360 cm^{-1}) and rotation (CO_r, 280 cm^{-1}) vibrations, OH_{ad} vibration on Cu (490 cm^{-1}), $Cu/ZnO_x/(OH)_y$ species (370 cm^{-1}) and Cu_2O species (405, 530, 610 cm^{-1}) obtained by fitting the intensities of the bands from the SERS spectra with respect to the applied potential and current density (top) during pulsed CO_2RR with $t_c = 4$ s and $t_a = 1$ s in CO_2-saturated 0.1 M $KHCO_3$. E_c is constant at -1.0 V, while **a,b**, are at $E_a = 0$ V and **c,d**, are at $E_a = 0.6$ V. **b,d**, show an extract of the full-time pulsed CO_2RR for better visibility.
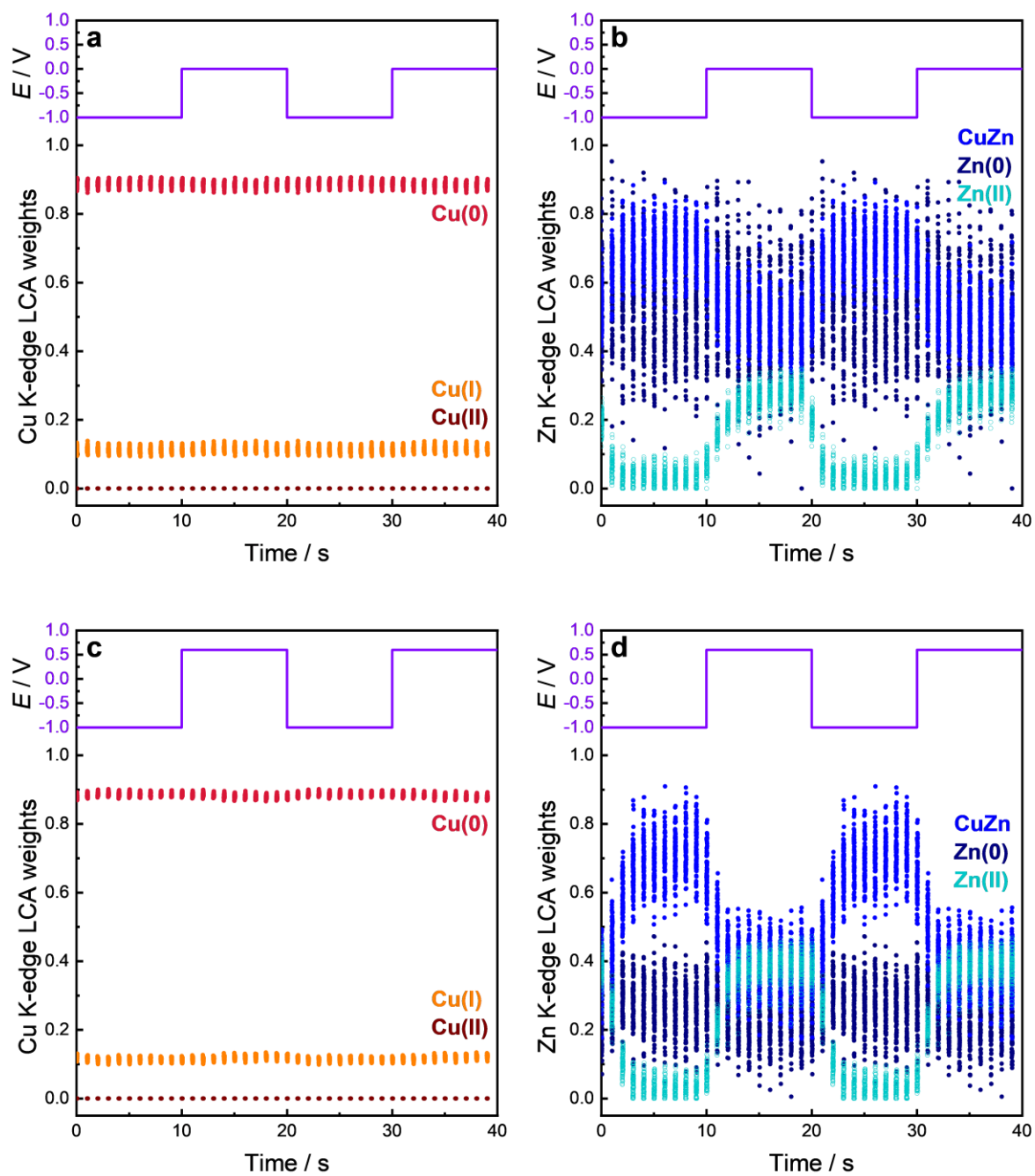
Figure S34. LCA-XANES analysis results of Cu and Zn, K-edges of pre-reduced Cu-Zn catalyst, averaged over one pulse sequence during pulsed CO_2RR with $t_c = t_a = 10$ s in CO_2-saturated 0.1 M $KHCO_3$. E_c is constant at -1.0 V, while **a,b**, are at $E_a = 0$ V and **c,d**, are at $E_a = 0.6$ V.
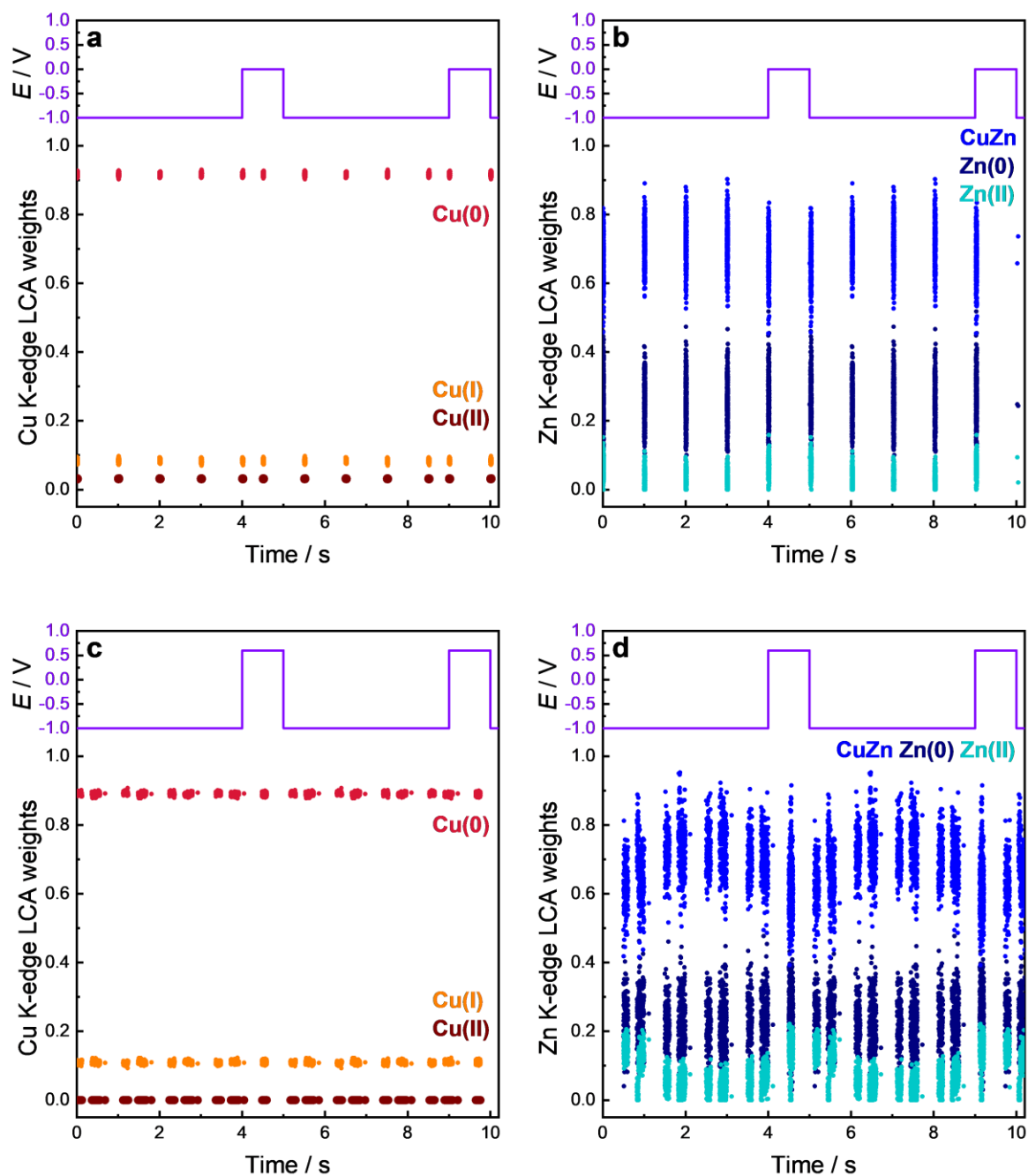
Figure S35. LCA-XANES analysis results of Cu and Zn, K-edge of pre-reduced Cu-Zn catalyst, averaged over one pulse sequence during pulsed CO_2RR with $t_c = 4$ s and $t_a = 1$ s in CO_2-saturated 0.1 M $KHCO_3$. E_c is constant at -1.0 V, while **a,b**, are at $E_a = 0$ V and **c,d**, are at $E_a = 0.6$ V.
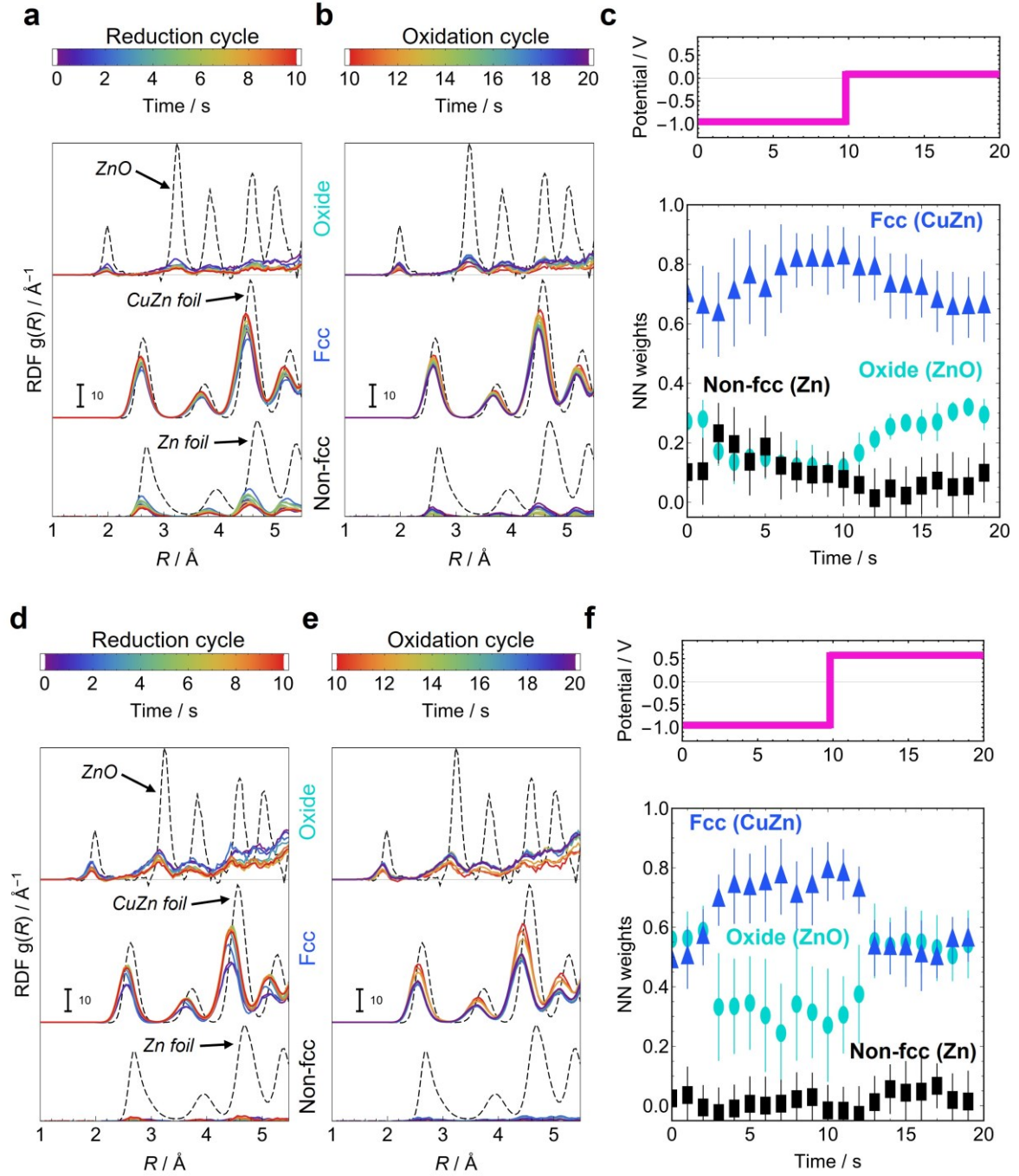
27

Figure S36. Averaged time-dependent evolution of the radial distribution functions *g(R)* and the concentrations obtained by the NN-EXAFS analysis from operando Zn K-edge EXAFS data during pulsed CO_2RR with $t_c = t_a = 10$ s in CO_2-saturated 0.1 M $KHCO_3$. The partial RDFs correspond to an oxide phase, an fcc-type Cu-Zn alloy phase, and a non-fcc-type phase Zn-rich face. **a,b**, RDFs during the reduction and oxidation cycle, respectively, and **c**, NN weights at E_c = -1.0 V and E_a = 0 V. **d,e**, RDFs during the reduction and oxidation cycle, respectively, and **f**, NN weights at E_c = -1.0 V and E_a = 0.6 V. For clarity the RDFs are shifted vertically.
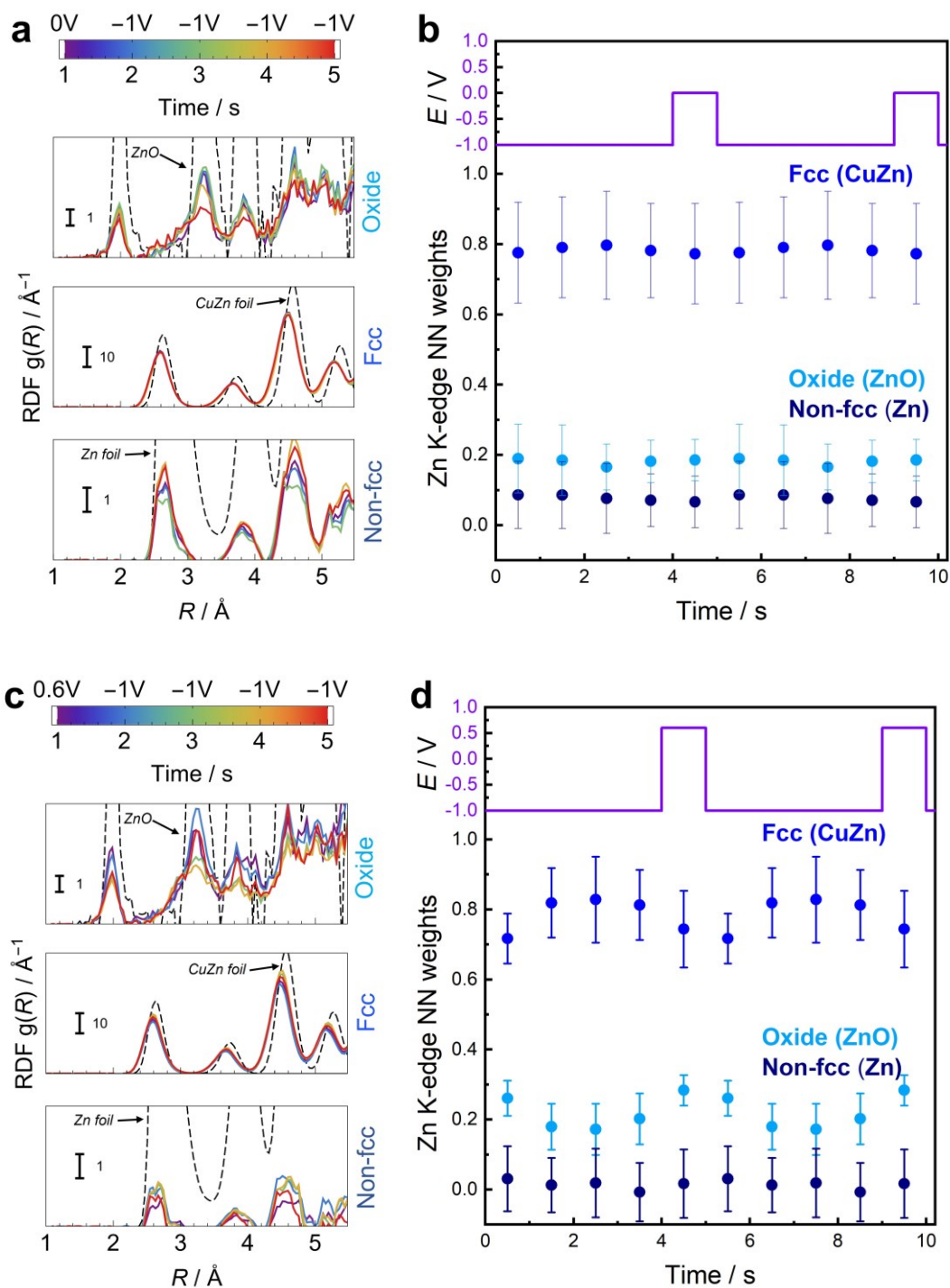
Figure S37. Averaged time-dependent evolution of the radial distribution functions *g(R)* (RDFs) and the concentrations obtained by the NN-EXAFS analysis from operando Zn K-edge EXAFS data during pulsed CO$_2$RR with t_c = 4 s and t_a = 1 s in CO$_2$-saturated 0.1 M KHCO$_3$. The partial RDFs correspond to an Zn oxide phase, an Cu-Zn fcc-type phase, and a non-fcc-type Zn-rich phase. **a**, RDFs during the reduction and oxidation cycle, and **b**, NN weights at E_c = -1.0 V and E_a = 0 V. **c**, RDFs during the reduction and oxidation cycle, and **d**, NN weights at E_c = -1.0 V and E_a = 0.6 V. For clarity the RDFs are shifted vertically.
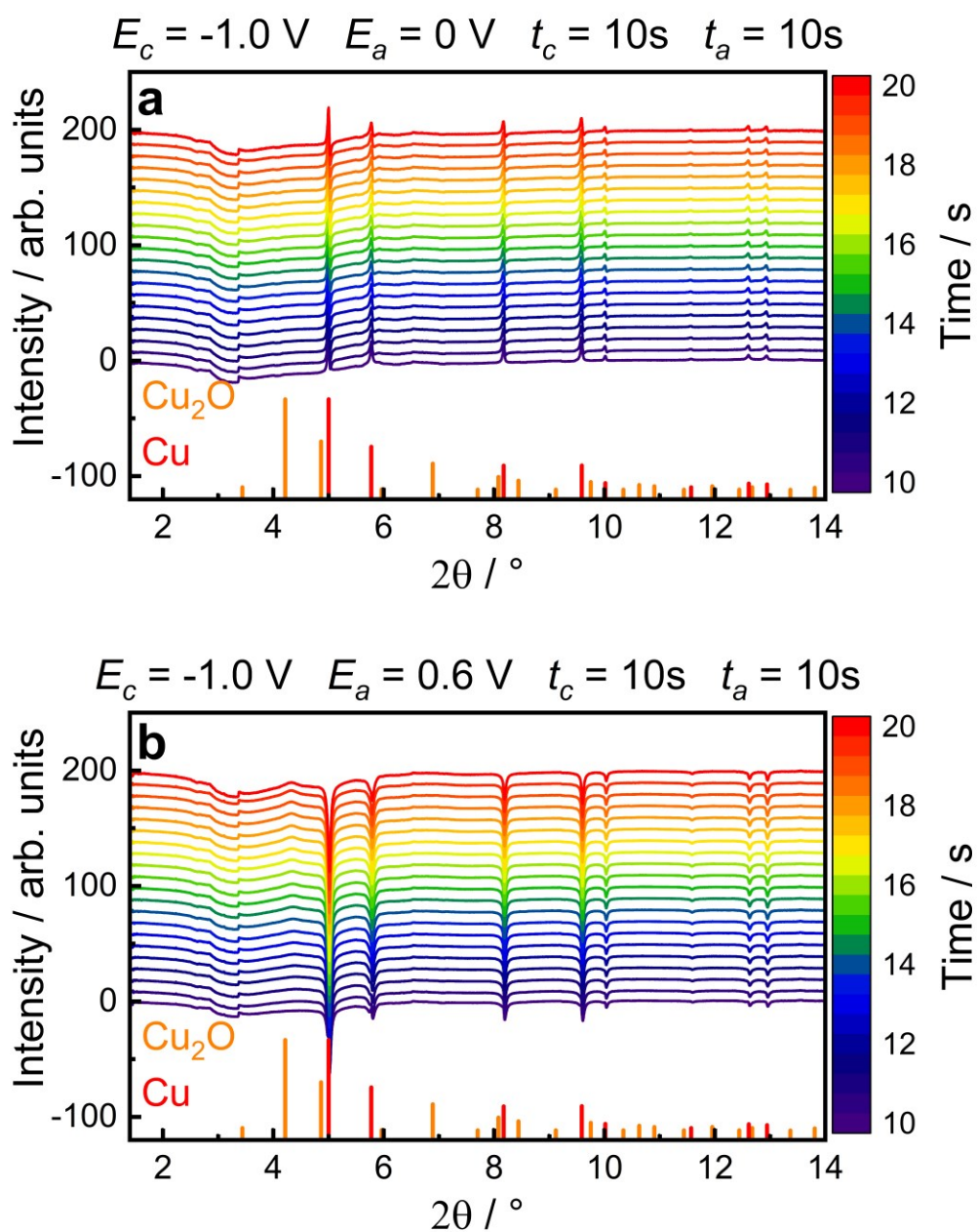
Figure S38. Evolution of the differential HE-XRD patterns of the pre-reduced Cu-Zn catalyst during the anodic pulse with $t_c = t_a = 10$ s and **a**, $E_a = 0$ V and **b**, 0.6 V in CO_2-saturated 0.1 M $KHCO_3$. The averaged diffraction patterns during the anodic pulse ($t = 10$-20 s) are subtracted from the averaged time-dependent diffraction pattern collected under pulsed CO_2RR conditions.
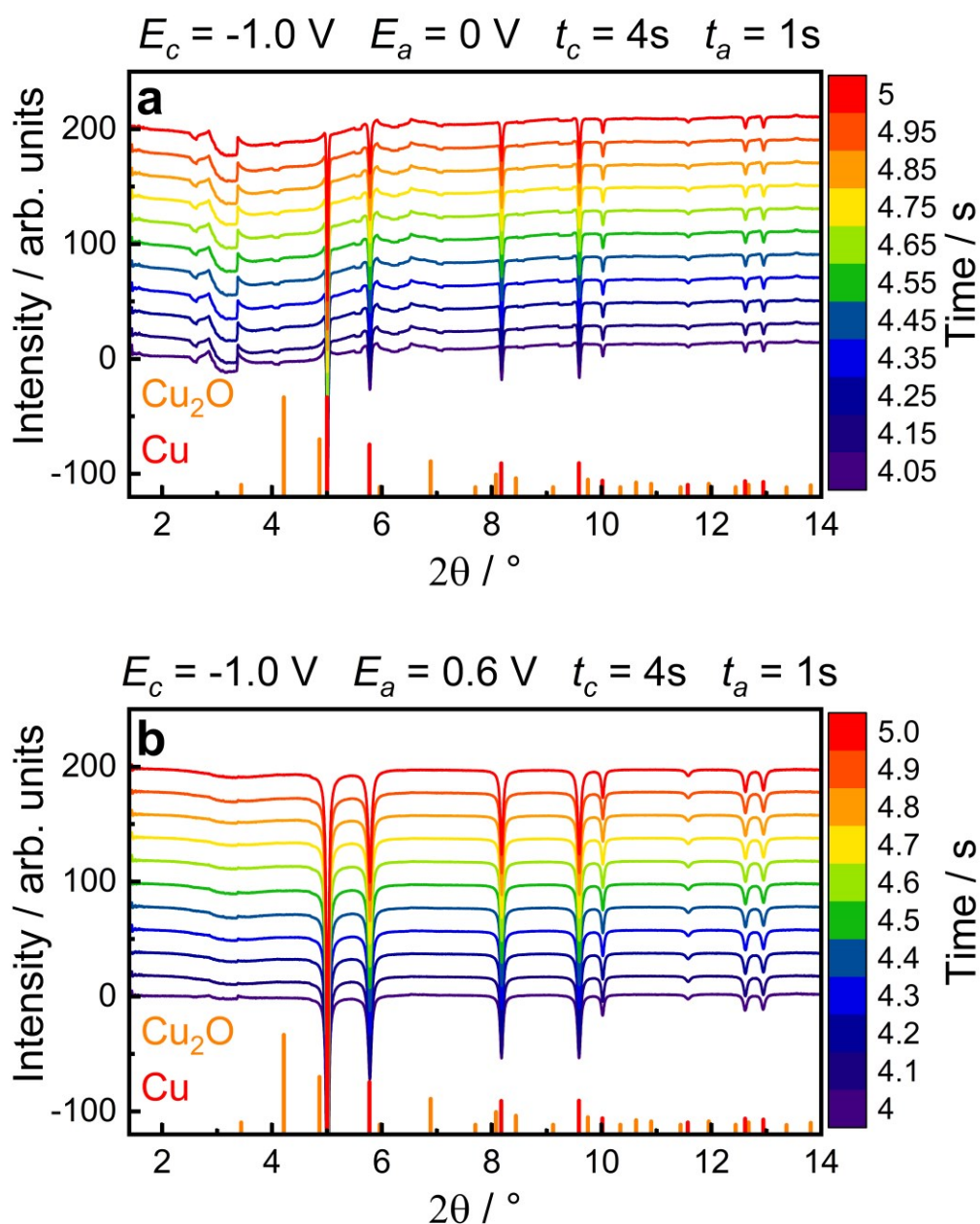
Figure S39. Evolution of the differential HE-XRD patterns of the pre-reduced Cu-Zn catalyst during the anodic pulse with t_c = 4 s and t_a = 1 s at **a**, E_a = 0 V and **b**, 0.6 V in CO_2-saturated 0.1 M $KHCO_3$. The averaged diffraction patterns during the anodic pulse (t = 10-20 s) are subtracted from the averaged time-dependent diffraction pattern collected under pulsed CO_2RR conditions.

Figure S40. Evolution of the averaged SERS spectra of the pre-reduced Cu-Zn catalyst from 150-1200 cm^{-1} during one pulse sequence with **a,b**, $t_c = t_a = 10$ s and **c,d**, $t_c = 4$ s and $t_a = 1$ s with $E_a = 0$ V and 0.6 V in CO$_2$-saturated 0.1 M KHCO$_3$. Characteristic bands are marked.
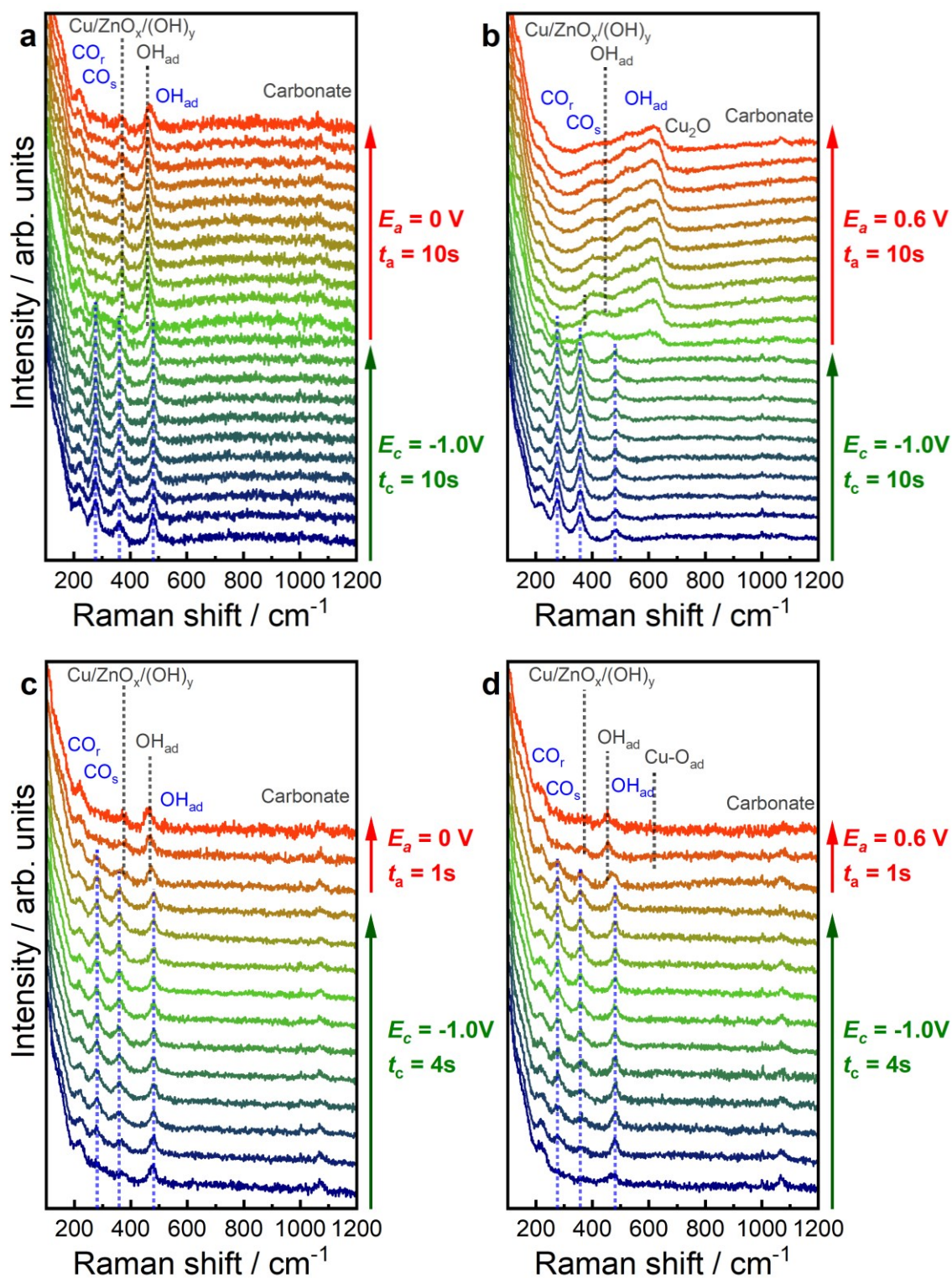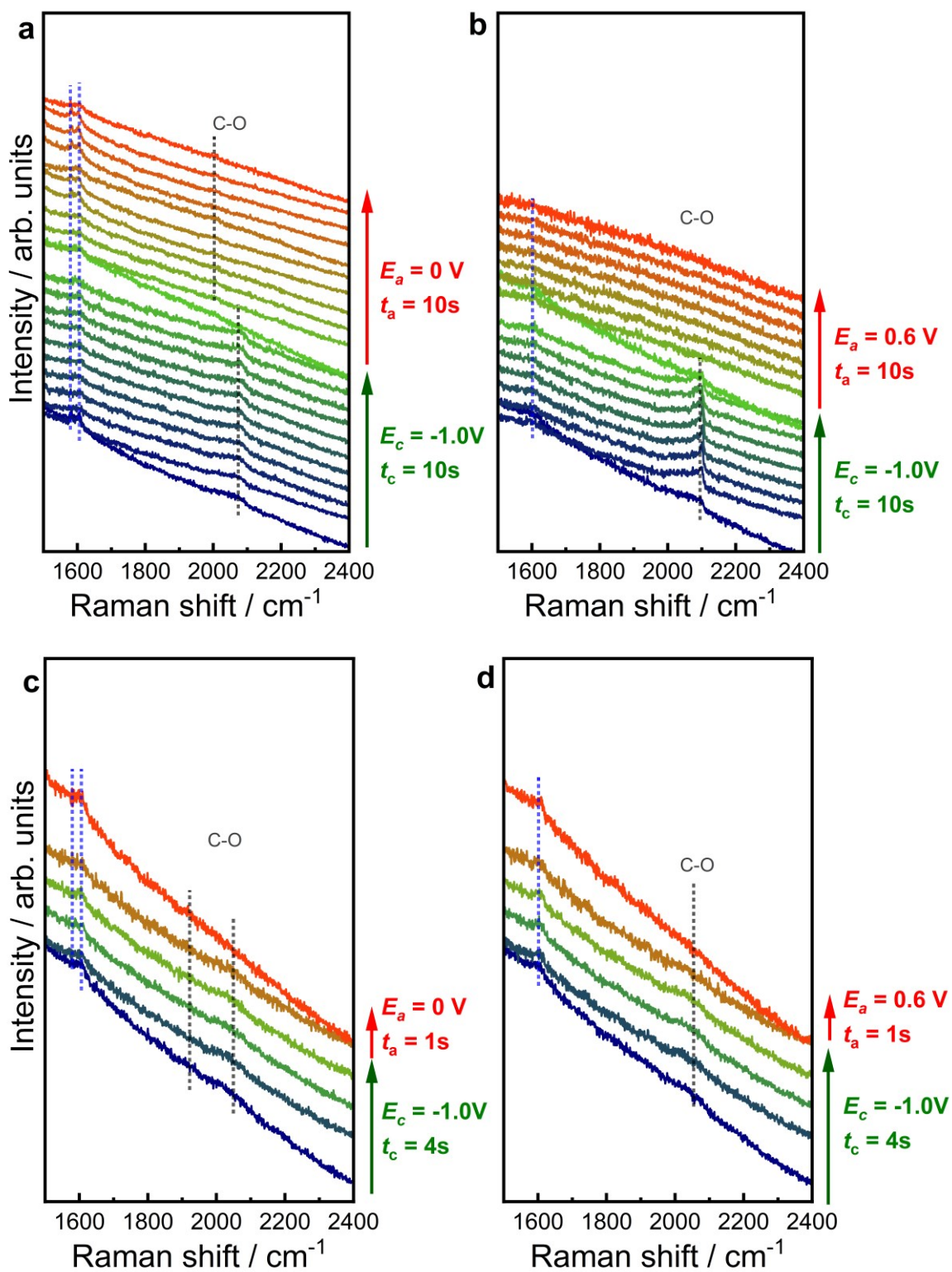
Figure S41. Evolution of the averaged SERS spectra of the pre-reduced Cu-Zn catalyst from 1500-2400 cm^{-1} during one pulse sequence with **a,b**, $t_c = t_a = 10$ s and **c,d**, $t_c = 4$ s and $t_a = 1$ s with $E_a = 0$ V and 0.6 V in CO$_2$-saturated 0.1 M KHCO$_3$. Characteristic bands are marked.
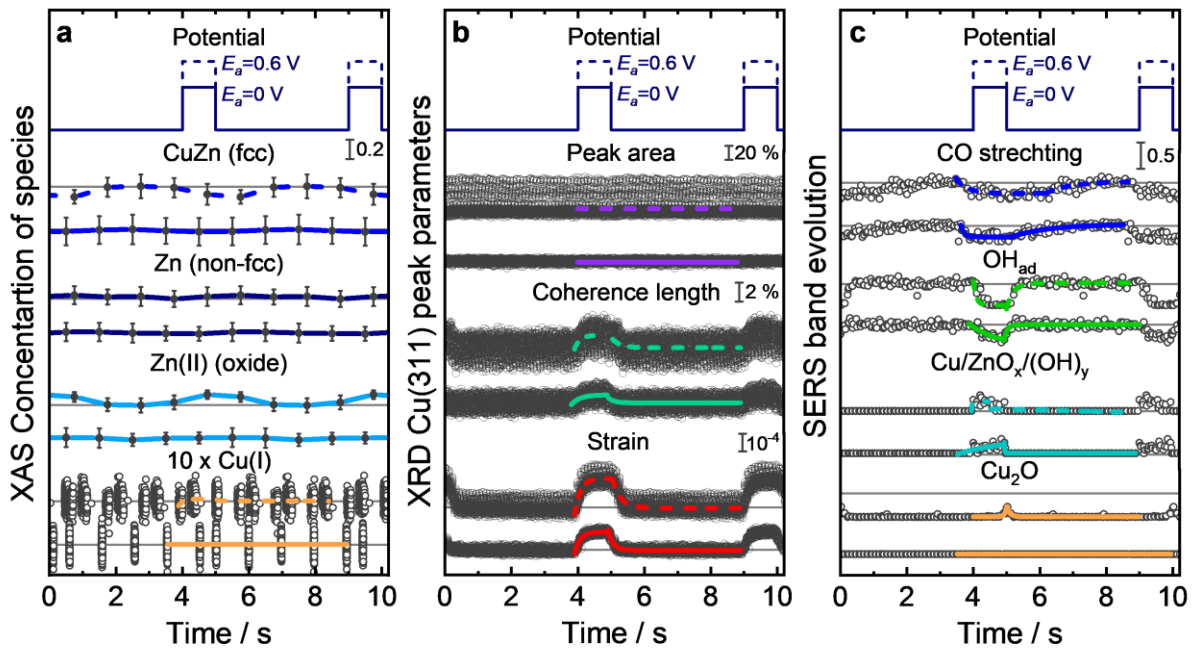
Figure S42. Averaged changes in the structure and adsorbates during a pulse sequence with E_c = -1.0 V and E_a = 0 V (bottom) or E_a = 0.6 V (top) for t_c = 4 s and t_a = 1 s by operando measurements in CO_2-saturated 0.1 M $KHCO_3$. **a**, ML-EXAFS analysis results for the Zn K-edge show the concentrations of different Zn species, and LCA-XANES analysis results for Cu K-edge show variations in Cu(I) concentration. The concentration profile of Cu(I) is multiplied by 10 for better visibility. **b**, HE-XRD Cu(311) Bragg peak parameters such as the relative changes in the Bragg peak area, the Cu coherence length, and the lattice strain. **c**, Raman band evolution of adsorbed CO (stretching band at 360 cm^{-1}), OH_{ad} (adsorbed on Cu at 490 cm^{-1}), Cu/ZnO$_x$/(OH)$_y$ species (370 cm^{-1}), and Cu_2O species (average of 530 and 620 cm^{-1}) obtained by fitting the intensities of the bands from the SERS spectra. The colored lines are exponential fits, and the solid lines represent the anodic pulse to 0 V, and the dashed lines the anodic pulse to 0.6 V. The solid grey lines indicate the respective values for each parameter at the end of the cathodic pulse.
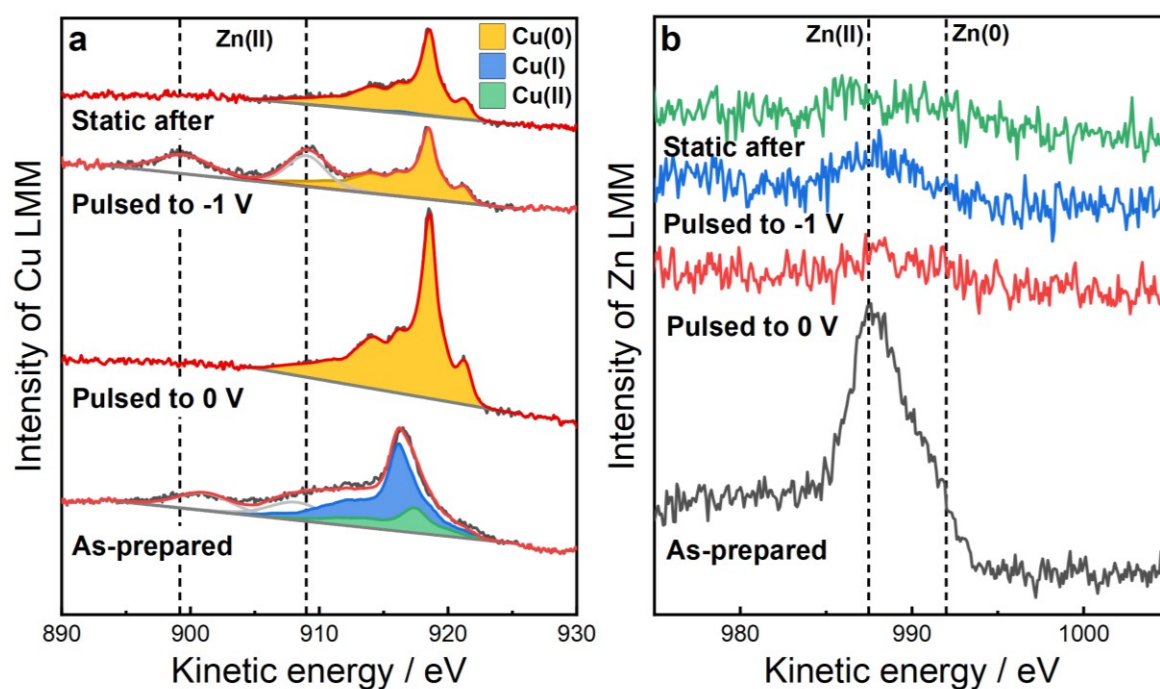
Figure S43. a, Quasi-in situ Cu LMM and **b**, Zn LMM Auger spectra of the Cu-Zn catalyst during different conditions in CO_2-saturated 0.1 M $KHCO_3$. Spectra for samples are compared where the pulse sequence ($t_c = 4$ s and $t_a = 1$ s, $E_a = 0$ V) was interrupted at the cathodic or anodic pulse. Zn(II) peaks in Cu LMM correspond to the [1]P and [3]P final state of Zn LMM.
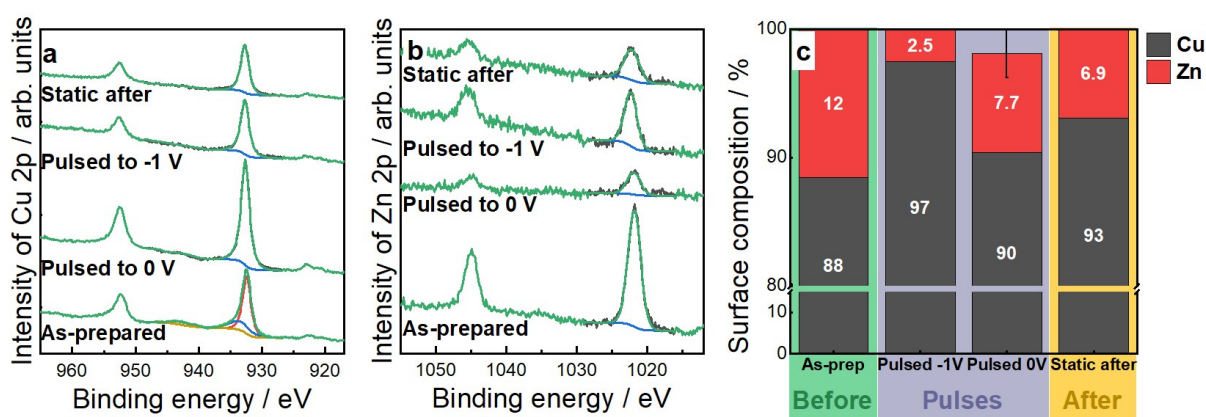

Figure S44. a, Quasi-in situ Cu 2p and **b**, Zn 2p core level regions of the Cu-Zn catalyst as well as **c**, the surface composition during different conditions. Spectra for samples are compared where the pulse sequence ($t_c = 4$ s and $t_a = 1$ s, $E_a = 0$ V in CO_2-saturated 0.1 M $KHCO_3$) was interrupted at the cathodic or anodic pulse. We also note here that the increase in the Cu:Zn ratio might also be related to the dissolution of the unstable Zn(II) species. In fact, ICP-MS measurements of the electrolyte indicate an increasing dissolution of Zn with higher E_a values (**Table S7**). However, at $E_a = 0$ V, the loss of Zn was only 10 %, and thus, surface segregation is likely to be the main reason for the detected change in surface composition.
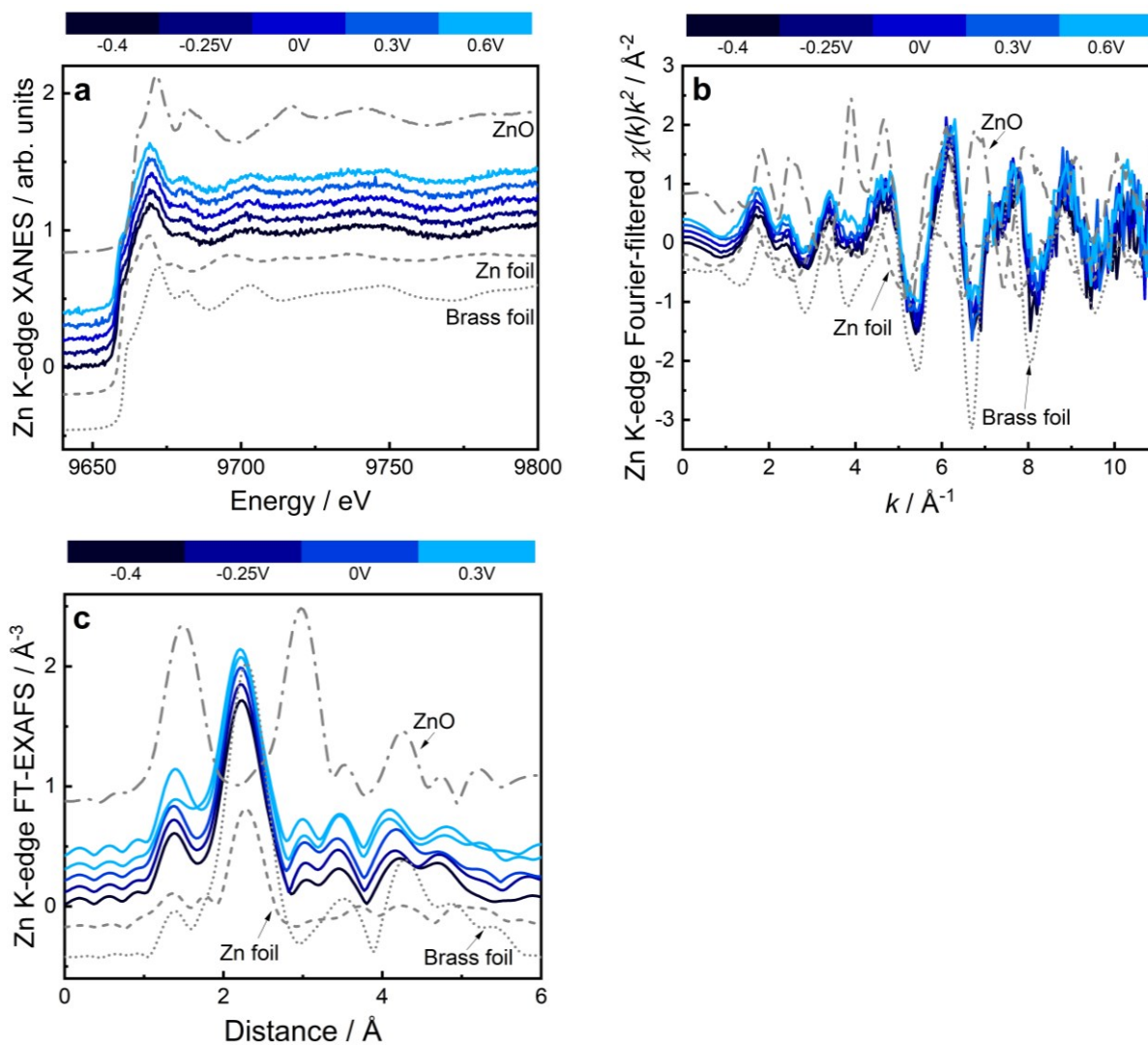
Figure S45. "Slow" (standard temporal resolution) operando Zn K-edge **a**, XANES, **b**, k-space, and **c**, EXAFS data during pulsed CO_2RR with $t_c = 4$ s and $t_a = 1$ s at different E_a values, while $E_c = -1.0$ V in CO_2-saturated 0.1 M $KHCO_3$. All data is shown with an offset in the y-axis.

Figure S46. RDFs obtained by the NN-EXAFS analysis from operando Zn K-edge EXAFS data during pulsed CO$_2$RR with $t_c = 4$ s and $t_a = 1$ s at different E_a values, while $E_c = -1.0$ V in CO$_2$-saturated 0.1 M KHCO$_3$. The partial RDFs correspond to an oxide phase, an fcc-type phase, and a non-fcc-type phase. **a**, RDFs are shifted vertically for clarity. **b**, shows excerpts of enlarged RDFs.

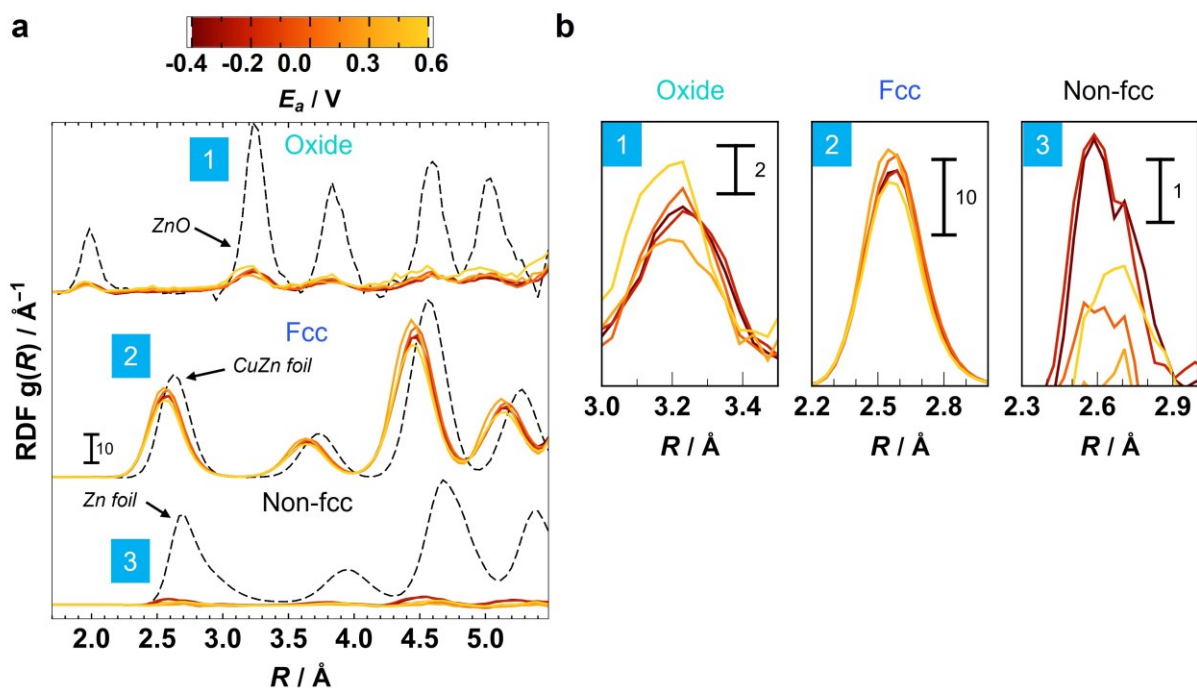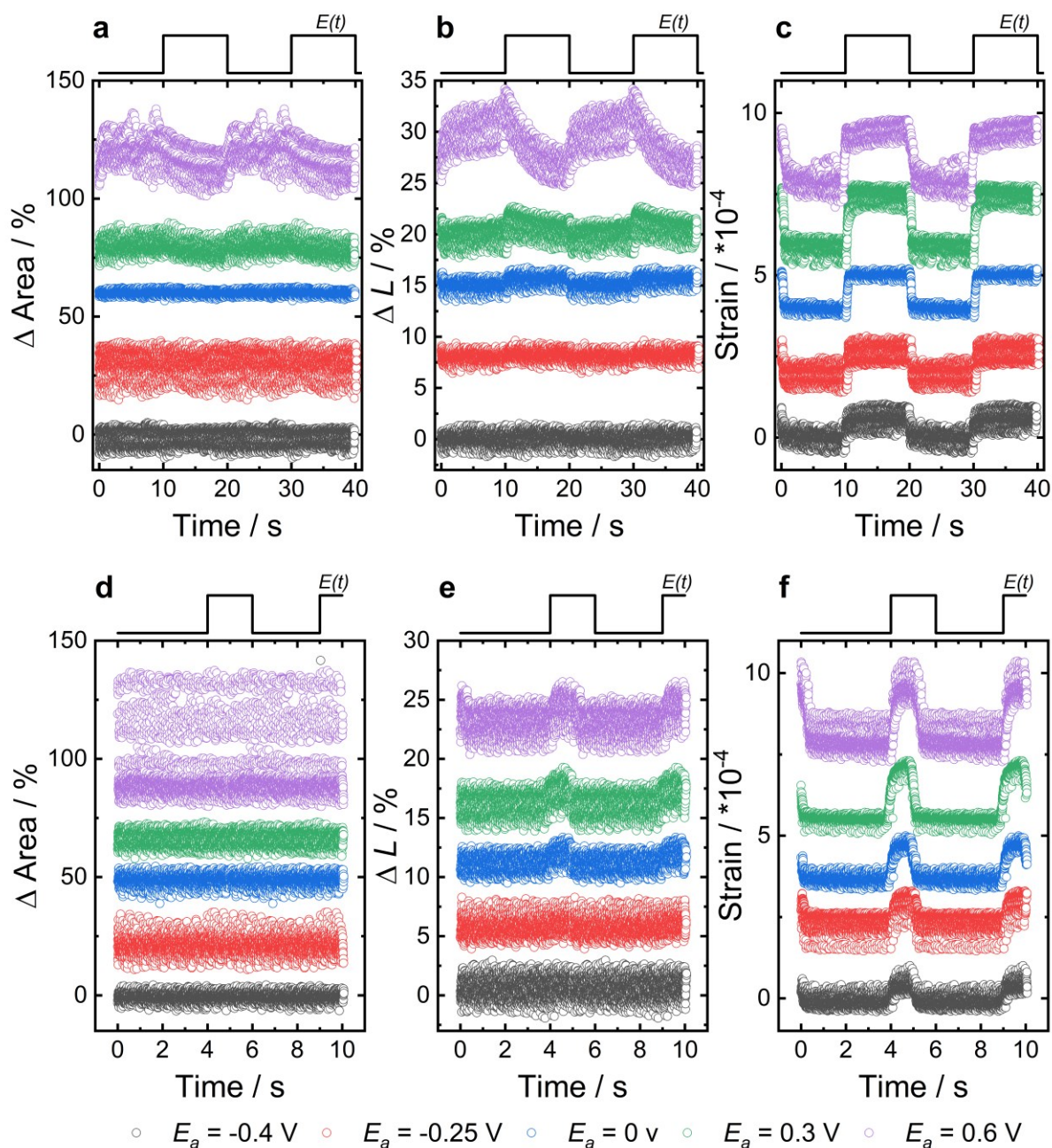**Figure S47.** Averaged changes of the Cu(311) Bragg peak parameters during a pulse sequence with E_c = -1.0 V and E_a = -0.4 V (black), -0.25 V (red), 0 V (blue), 0.3 V (green) and 0.6 V (purple) for different time lengths by operando HE-XRD in CO_2-saturated 0.1 M KHCO$_3$. **a**, Relative changes in the Bragg peak area, **b**, the Cu coherence length, and **c**, the lattice strain for $t_c = t_a = 10$ s. **d**, Relative changes in the Bragg peak area, **e**, the Cu coherence length, and **f**, the lattice strain for $t_c = 4$ s and $t_a = 1$ s.

Figure S48. Evolution of the averaged SERS spectra of the pre-reduced Cu-Zn catalyst from 150-1200 cm^{-1} during one pulse sequence with $t_c = t_a = 10$ s at **a**, $E_a = +0.3$ V, at **b**, $E_a = -0.25$ V and at **c**, $E_a = -0.4$ V in CO$_2$-saturated 0.1 M KHCO$_3$. Characteristic bands are marked.

Supplementary Tables

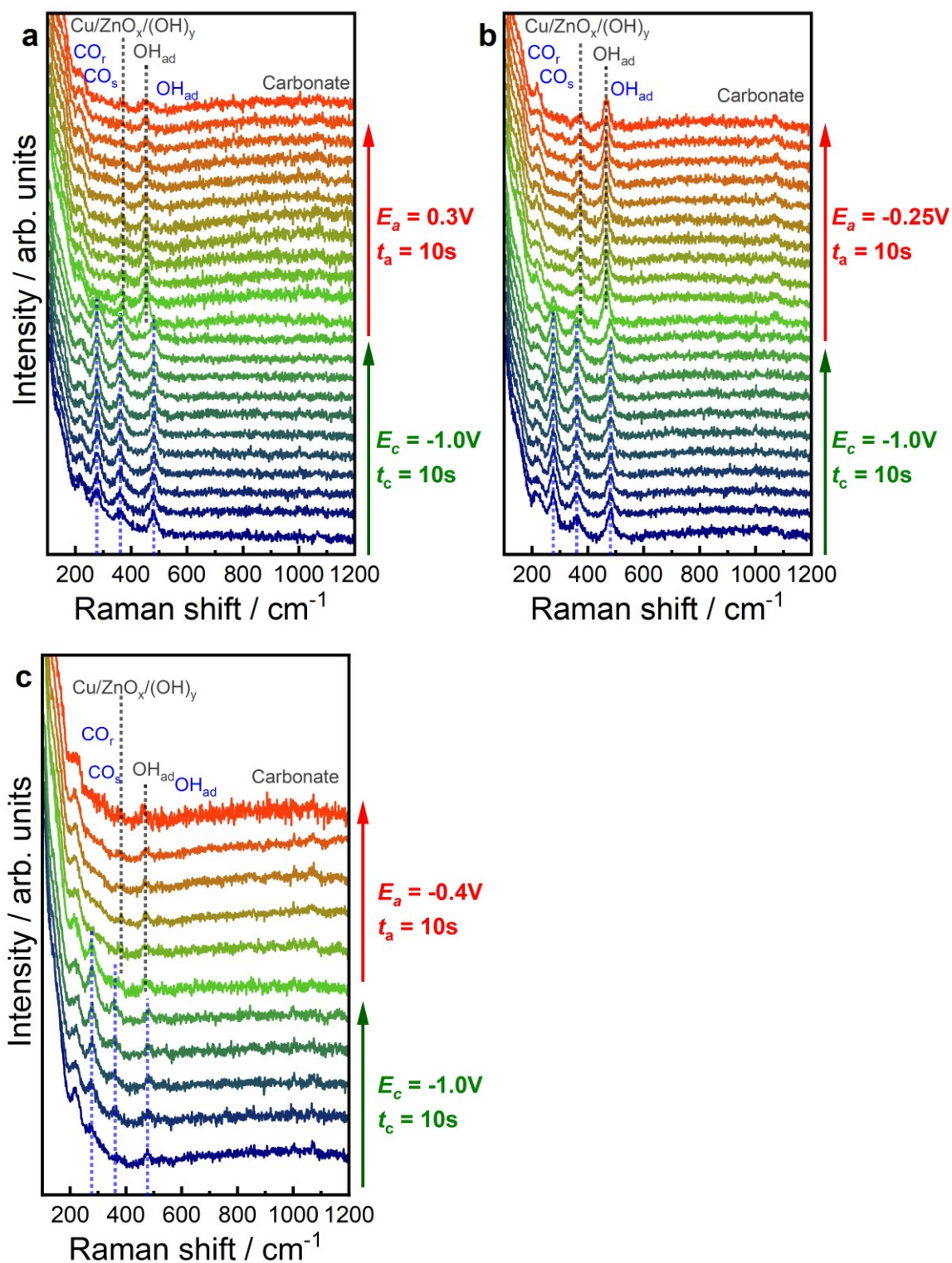**Table S1.** Edge lengths and corresponding size distribution of Cu-Zn obtained from the analysis of STEM images in the as-prepared state, after 1 h of static CO_2RR, and after different pulse protocols with fixed E_c = -1.0 V, t_c = 4 s and t_a = 1 s in CO_2-saturated 0.1 M $KHCO_3$.

Sample	Edge length / Particle diameter of Cu [nm]	Length of Zn [nm]
As-prepared	20(3)	2.0(5) (Edges)
Static at -1.0 V	24(4)	4.0(6) (Particles)
Pulsed with E_a = 0 V	24(5)	5(1) (Particles)
Pulsed with E_a = 0.6 V	28(5)	21(8) (Islands)

Table S2. Elemental quantification of Cu and Zn extracted from the STEM-EDX images of **Fig. 1** of Cu-Zn in the as-prepared state, after 1 h of static CO_2RR and after different pulse protocols with fixed E_c = -1.0 V, t_c = 4 s and t_a = 1 s, while E_a was varied in CO_2-saturated 0.1 M $KHCO_3$.

Sample	Cu [%]	Zn [%]
As-prepared	93.6(8)	6.4(8)
Static at -1.0 V	95.8(6)	4.2(6)
Pulsed with E_a = 0 V	97.1(4)	3.0(4)
Pulsed with E_a = 0.6 V	96.1(5)	3.9(5)

Table S3. Cu and Zn composition of as-prepared Zn/Cu_2O NCs (powder) obtained by ICP-MS.

Sample	Cu [at%]	Zn [at%]
As-prepared	93.5(7)	6.5(7)

Table S4. Edge lengths and corresponding size distribution of Cu-Zn obtained from the analysis of SEM images in as-prepared state, after 1 h of static CO_2RR and after different pulse protocols (different E_a), but with fixed E_c = -1.0 V, t_c = 4 s and t_a = 1 s in CO_2-saturated 0.1 M $KHCO_3$.

Sample	Edge length [nm]
As-prepared	23(4)
Static at -1.0 V	26(6)
Pulsed with E_a = -0.4 V	27(5)
Pulsed with E_a = -0.25 V	26(6)
Pulsed with E_a = 0 V	27(6)
Pulsed with E_a = 0.3 V	33(8)
Pulsed with E_a = 0.6 V	35(6)

Table S5. Edge lengths and corresponding size distribution of the bare Cu_2O cubes obtained from the analysis of STEM images in as-prepared state, after 1 h of static CO_2RR and after 1 h of pulsed CO_2RR at E_a = 0 V (E_c = -1.0 V, t_c = 4 s and t_a = 1 s).

Sample	Edge length of Cu [nm]
As-prepared	24(4)
Static at -1.0 V	27(6)
Pulsed with E_a = 0 V	35(6)

Table S6. Composition of Cu and Zn in the as-prepared state and after 1 h of static CO_2RR of the Cu-Zn catalyst obtained by the comparison of the 2p quasi-in situ XPS spectra (shown in **Fig. S15**).

Sample	Cu 2p [at%]	Zn 2p [at%]
As-prepared	85(2)	15(1)
Static after -1.0 V	90(1)	10(1)

Table S7. Cu and Zn mass and composition of Cu-Zn catalyst in the electrolyte by ICP-MS measurements after 1 h of different reaction conditions.

Sample	m_{Cu} [µg]	Cu [at%]	m_{Zn} [µg]	Zn [at%]
Static at -1.0 V	0.62(8)	0.44(5)	0.13(2)	1.4(3)
Pulsed to -0.4 V	0.355(2)	0.253(2)	0.51(1)	5.5(5)
Pulsed to -0.25 V	0.683(3)	0.488(3)	1.044(1)	1.044(1)
Pulsed to 0 V	0.3158(9)	0.2256(7)	0.994(6)	10.75(7)
Pulsed to 0.3 V	0.997(4)	0.712(3)	2.239(5)	24.20(5)
Pulsed to 0.6 V	1.457(1)	1.0407(9)	1.914(6)	20.70(6)

Supplementary References

(1) Timoshenko, J.; Bergmann, A.; Rettenmaier, C.; Herzog, A.; Arán-Ais, R. M.; Jeon, H. S.; Haase, F. T.; Hejral, U.; Grosse, P.; Kühl, S.; Davis, E. M.; Tian, J.; Magnussen, O.; Roldan Cuenya, B., Steering the structure and selectivity of CO2 electroreduction catalysts by potential pulses. *Nat. Catal.* **2022,** *5*, 259-267.

(2) Rüscher, M.; Herzog, A.; Timoshenko, J.; Jeon, H. S.; Frandsen, W.; Kühl, S.; Roldan Cuenya, B., Tracking heterogeneous structural motifs and the redox behaviour of copper–zinc nanocatalysts for the electrocatalytic CO2 reduction using operando time resolved spectroscopy and machine learning. *Catal. Sci. Technol.* **2022,** *12*, 3028-3043.

(3) Schmitt, K. G.; Gewirth, A. A., In Situ Surface-Enhanced Raman Spectroscopy of the Electrochemical Reduction of Carbon Dioxide on Silver with 3,5-Diamino-1,2,4-Triazole. *J. Phys. Chem. C* **2014,** *118*, 17567-17576.

(4) Kottakkat, T.; Klingan, K.; Jiang, S.; Jovanov, Z. P.; Davies, V. H.; El-Nagar, G. A. M.; Dau, H.; Roth, C., Electrodeposited AgCu Foam Catalysts for Enhanced Reduction of CO2 to CO. *ACS Appl. Mater. Interfaces* **2019,** *11*, 14734-14744.